Research & Design

Volume 1 Issue 1

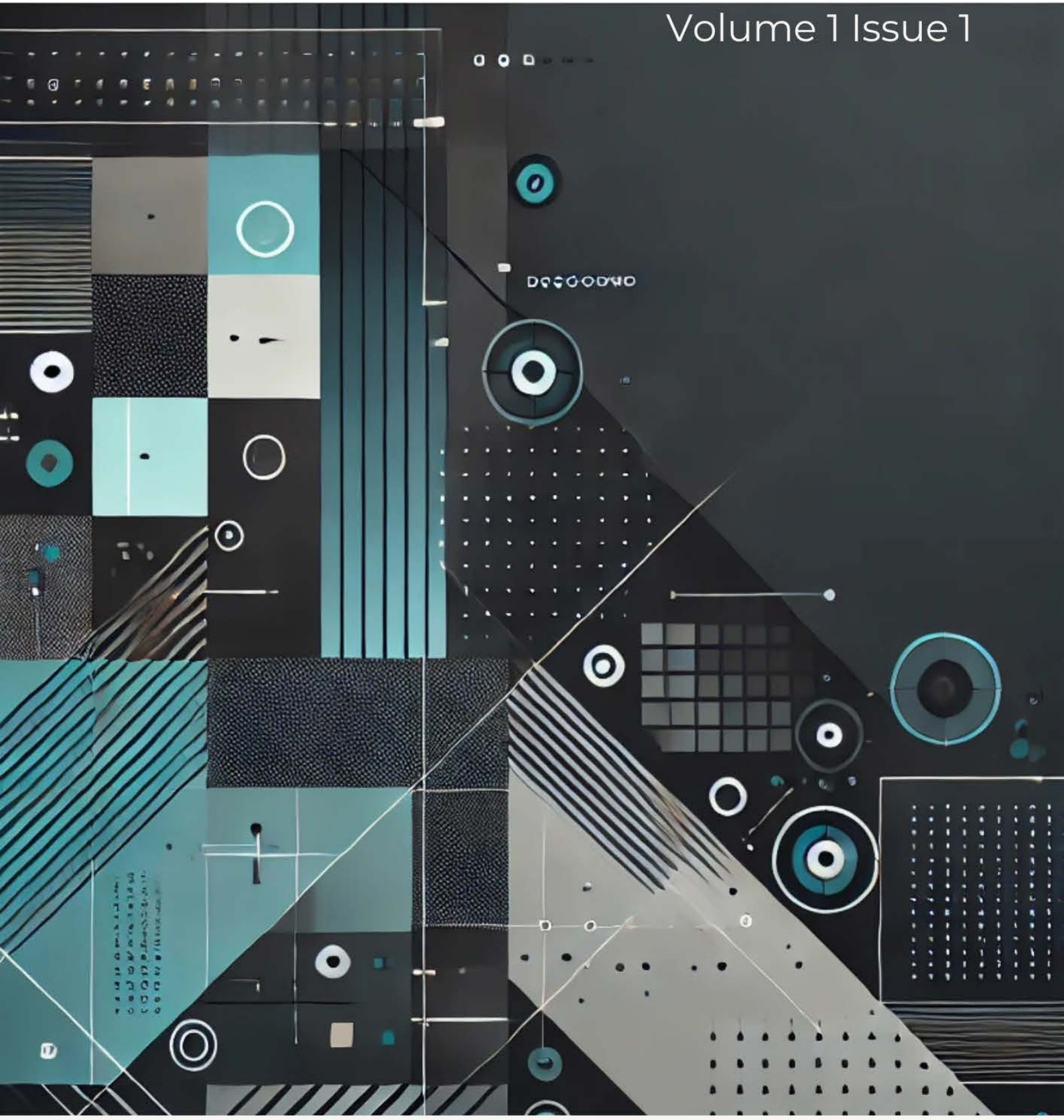

MIM Research & Publishing

Research & Design (REDE) is a multidisciplinary, peer-reviewed, open-access journal committed to bridging the gap between research and design. Inspired by the fundamental problem-solving mechanisms of science, REDE fosters innovation by publishing studies that connect theoretical exploration with practical applications. Our mission is to advance knowledge and provide a platform where research-driven solutions meet real-world challenges.

Supported by the MIM Research Group, **REDE offers a free and open-access publication model**, ensuring that all published articles are freely available to the global research community. Authors are not required to pay any fees, reflecting the journal's dedication to inclusivity and equitable knowledge dissemination.

The journal welcomes contributions from diverse disciplines, emphasizing the interconnectedness of research and design across various fields. Original research articles, reviews, technical notes, and short communications that address complex societal issues are encouraged. Each submission undergoes a rigorous peer-review process to ensure academic excellence and impact.

REDE covers a wide array of fields, reflecting its commitment to multidisciplinary collaboration. From traditional engineering disciplines to contemporary topics like gamification and data science, the journal provides a home for innovative studies that address modern challenges.

We invite you to explore our diverse content and contribute to advancing research and design in your field.

The topics covered in REDE include:

- Aesthetics
- Built Environment
- Economics and Finance
- Social Sciences
- Engineering Sciences
- Data Science
- Game & Gamification
- Industrial Design
- Interface Design

Abstracting and Indexing
Please visit http://www.jrede.org/ for more information.

The journal of

RESEARCH & DESIGN

MIM Research Group

Research & Design

www.jrede.org

Editorial Board

Research & Design
www.jrede.org

Editorial Board Members

MIM Research Group
Research & Design
www.jrede.org

In This Issue

Research & Design
MIM Research Group Publications

http://www.jrede.org/

MIM Research Group Research & Design
www.jrede.org

Research Article

Effect of concrete strength and detailing properties on seismic damage for RC structures

Hayri Baytan Ozmen*[1a], Mehmet Inel[2b]

[1]*Department of Civil Engineering, Usak University, Usak, Turkey.*
[2]*Department of Civil Engineering, Pamukkale University, Denizli, Turkey.*

Article Info

Article History:

Received: 20 Oct 2024

Accepted: 2 Dec 2024

Keywords:

Concrete strength;
Lateral reinforcement;
Nonlinear analysis;
Seismic code;
Seismic performance

Abstract

This study investigates the effects of concrete strength, lateral reinforcement detailing and design code on the seismic performance of reinforced concrete (RC) buildings representative of existing residential structures. A total of 48 nonlinear inelastic models of 2, 4, and 7 storey buildings, designed per the 1975 and 1998 Turkish seismic codes, were analyzed using nonlinear static and dynamic methods. Capacity curves were obtained through inelastic static analysis, while displacement demands were calculated for 264 ground motion records using nonlinear dynamic analysis. The exceedance ratios of performance levels—Immediate Occupancy (IO), Life Safety (LS), and Collapse Prevention (CP)—were determined based on these demands. The findings reveal that the IO performance level is minimally affected by variations in material properties and detailing, as it primarily depends on structural strength. Paradoxically, in low-rise buildings, increased concrete strength and reinforcement can lead to higher IO exceedance ratios due to increased longitudinal reinforcement elongation at lower curvature values. The damage rate was found to be high in 4-storey buildings designed under the 1975 code showing higher exceedance ratios than 7-storey buildings due to relatively weaker structural systems and construction practices. In contrast, buildings designed per the 1998 code exhibited significantly lower exceedance ratios, highlighting the effectiveness of modern seismic design standards. The results underscore the importance of seismic detailing and retrofitting older buildings to improve resilience. This study may provide insights into the seismic behavior of RC buildings, offering guidance for structural engineers and policymakers in enhancing building safety.

1. Introduction

The seismic performance of reinforced concrete (RC) structures is a critical area of study in civil engineering, particularly in regions prone to earthquakes. The ability of these structures to withstand seismic forces is significantly influenced by various factors, including concrete strength, lateral reinforcement amount, and spacing. These factors may be considered as key parameters for the design of new structures or evaluation of existing ones. Concrete strength plays a pivotal role in determining the overall load-bearing capacity and ductility of RC elements. Higher concrete strength generally enhances the structural integrity and resilience of buildings during seismic events, as it allows for better energy dissipation and reduced deformation under lateral loads [1–3]. However, the effectiveness of increased concrete strength is dependent upon the adequacy of lateral

*Corresponding author: baytan.ozmen@usak.edu.tr
[a]orcid.org/ 0000-0001-6750-8632; [b]orcid.org/ 0000-0002-8323-259X;
DOI: http://dx.doi.org/10.17515/rede2024.005en1124rs

reinforcement, which serves to confine the concrete and allows the increased capacity to be effective by increased ductility.

Lateral reinforcement, typically in the form of stirrups or ties, is essential for enhancing the ductility and energy absorption capacity of RC structures. The spacing and amount of this reinforcement directly affect the confinement of the concrete core, which is critical for maintaining structural performance under seismic loading. Research has shown that insufficient lateral reinforcement spacing can lead to inadequate confinement, resulting in reduced load-carrying capacity and increased vulnerability to seismic damage [4]. For instance, studies have indicated that widely spaced transverse reinforcement can compromise the structural integrity of RC columns, leading to significant failures during seismic events [5]. Therefore, optimizing the amount and spacing of lateral reinforcement is crucial for improving the seismic resilience of RC structures.

The interaction between concrete strength and lateral reinforcement is complex and requires careful consideration in design practices. Analytical models and experimental studies have demonstrated that the combination of high concrete strength and appropriate lateral reinforcement can significantly enhance the seismic performance of RC columns and frames [6, 7]. For example, the use of high-strength steel bars in conjunction with high-strength concrete has been shown to improve the overall ductility and energy dissipation capabilities of RC elements, thereby reducing the likelihood of catastrophic failure during earthquakes [8, 9]. Furthermore, the design of lateral reinforcement must account for various factors, including axial loads and the specific seismic design category of the structure, to ensure that the reinforcement effectively contributes to the overall stability and resilience of the building [10, 11].

The moment-curvature relationship, which describes how a beam or column deforms under bending, is influenced by both the amount of reinforcement and the concrete strength [7, 12]. Structures with well-designed reinforcement layouts tend to exhibit more favorable moment-curvature characteristics, enabling them to withstand larger deformations without experiencing significant damage [13, 14]. This is particularly important in the context of modern seismic design, where the goal is to ensure that structures can endure substantial forces while maintaining their integrity and functionality.

The implications of these interactions extend beyond individual elements to the overall performance of entire structures. The seismic response of multi-storey buildings, for instance, is heavily influenced by the design and detailing of RC columns and beams, which must work in concert to provide adequate lateral stability [15–17]. As such, a comprehensive understanding of how concrete strength and lateral reinforcement affect seismic damage is essential for engineers tasked with designing safe and resilient structures. This understanding not only informs design codes and standards but also guides the development of innovative materials and reinforcement techniques aimed at enhancing the seismic performance of RC buildings.

The aim of the study is to evaluate the effect of concrete strength, seismic code and lateral reinforcement detailing properties on the behavior of reinforced concrete structures and seismic damage risk for different performance levels. For this purpose, 2, 4 and 7 storey reference buildings without any irregularities representing the existing building stock in Turkey were modeled as residential buildings according to the 1975 and 1998 codes [18, 19].

The building characteristics used in scope of the study were created through an inventory study on approximately 500 existing buildings. In scope of the study by Ozmen et. al [20],

the values of some structural properties that are thought to have an effect on the strength and strain behavior of reinforced concrete structures in the building stock were examined. The buildings were divided into subgroups according to their construction years and number of storeys and a total of 475 buildings and 40351 columns and 3123 beams selected from these buildings were taken into consideration. The properties of these buildings were converted into numerical values (column area/building area, partition wall amount/building area, element size and reinforcement amount, etc.). In this way, 2-storey building models representing 1-2 storey buildings, 4-storey building models for 3-5 storey buildings and 7-storey building models for 6 and more storey buildings were created in accordance with the average values of approximately 34 parameters reflecting existing building characteristics.

The year 1998 is important for Turkey being the year for a seismic code change and a corner for the common use of higher strength concrete in buildings. For each building group, two different earthquake codes (1975 and 1998), two different concrete compressive strengths and two different lateral reinforcement conditions were considered. Concrete compressive strength of 16 MPa (medium quality) and 10 MPa (low quality) for pre-1998 structures and 25 MPa (good quality) and 16 MPa (medium quality) for post-1998 are considered. For each model, two different lateral reinforcement conditions were taken into consideration: reinforcement arrangement in accordance with the regulations in the confinement zones and 200 mm spacing and without stirrups. For the infill walls, two different cases were analyzed, one in which the structures had an amount of load-bearing infill walls suitable for the inventory study and one in which the load-bearing properties of the infill walls were not taken into account. SAP2000 program was used in the analyses [21].

According to the 2018 Turkish Earthquake Code, the displacement capacity values of these models at the Immediate Occupancy (IO), Life Safety (LS) and Collapse Prevention (CP) performance levels are determined [22]. The capacity curves of the models were reduced to “Single Degree of Freedom” (SDOF) by bi-linearization [22]. Nonlinear displacement demands of the SDOF models were calculated by nonlinear time domain analysis using 264 real earthquake records with different peak ground acceleration values and soil properties. Using the seismic demand and capacity values of the models, we calculated the ratio of instances where the seismic demand exceeded the model capacities. This was done by dividing the number of earthquakes that surpassed the relevant capacity by the total number of earthquakes analyzed. Through the analyses conducted in this study, we quantitatively assessed how various parameters—such as the number of storeys, the building codes considered, the material types, and the detailing conditions—affect the damage rates at different earthquake intensities for each performance level of the buildings. The results obtained from this analysis can enhance methods for estimating earthquake damage and assist in prioritizing risk assessments for structures.

2. Modelling assumptions and model properties

In the study, 3-D modeling of a total of 48 buildings with 3 different plan and different values of the examined parameters were made. The plan views of the models are given in Fig 1. Considering the two principal directions of the buildings, 96 analysis results were evaluated within the scope of the study.

In order to determine the seismic behavior and performance of the considered buildings, nonlinear models were prepared in accordance with the 2018 Turkish seismic code [22]. Non-linear inelastic behavior was determined by means of plastic hinges placed at the ends

of the elements. In order to define a plastic hinge, the coordinates of points B, C, D, E (and IO, LS, CP for performance criteria) given in Fig. 2 should be determined.

To accurately assess the performance of flexural plastic hinges in reinforced concrete structures, it is essential to understand the moment-curvature relationship. This relationship describes how the curvature of a structural element changes in response to applied moments. To establish this relationship, the strain-strength characteristics of reinforced concrete must be evaluated at critical sections of each structural element. By analyzing these sections, we can determine how much deformation the flexural plastic hinges can endure before failure occurs. This analysis utilizes the moment-curvature relationship derived from the material's deformation-strength characteristics and established ductility criteria. The identification of flexural joints involves calculating the moment-curvature relationships for the critical sections of each member. This calculation is performed using specialized confinement analysis software developed by the authors, known as SEMAp [23]. This software allows for a detailed examination of how the confinement of concrete affects its performance under load, thereby providing numerical insights into the behavior of flexural joints in reinforced concrete structures.

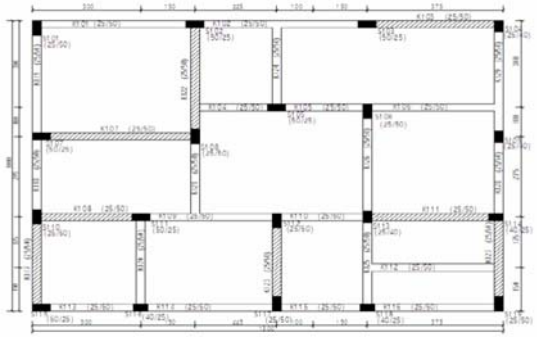

a) Two storey building plan

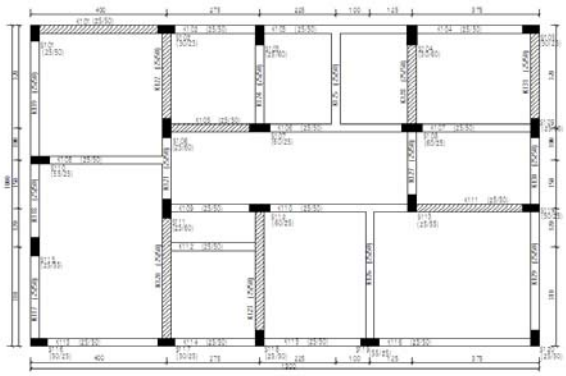

b) Four storey building plan

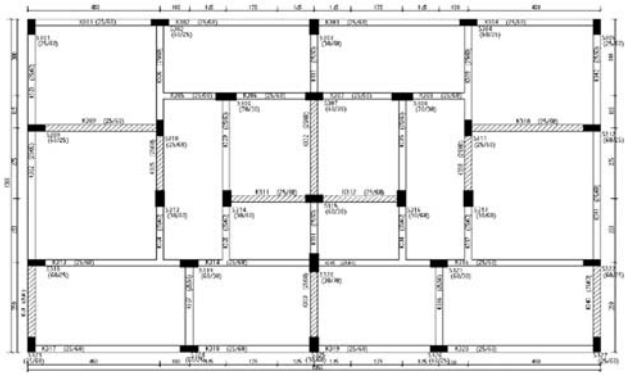

c) Seven storey building plan

Fig. 1. Plan views of the buildings considered in the study. Shaded areas represent walls with load bearing ability.

For concrete material, the Mander confined concrete model is used [24]. Using these moment-curvature relationships, ultimate deformation criteria and plastic joint length, the plastic rotational capacity and joint properties of each member were determined. Damage capacity limit values for flexural joints are given in Table 1.

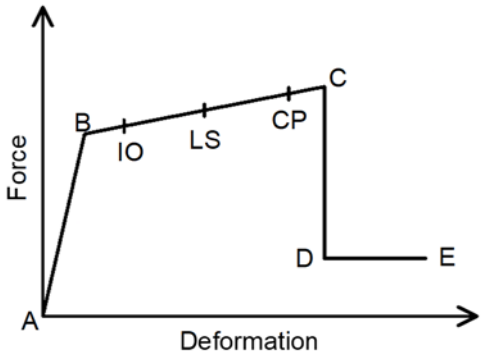

Fig. 2 Typical force and deformation relation of a plastic hinge

In addition to flexural joints, shear joints are also defined in columns and beams. Unlike flexural joints, no ductility is calculated for shear joints and it is assumed that the elements reach the collapse state as soon as they reach their shear capacity. Shear capacities were calculated according to TS500 [25]. In order to take into account the effect of the infill walls on the structural behavior of the structure, each model was prepared in two different forms, with and without considering the walls as load-bearing elements. The effect of the walls is reflected by using equivalent diagonal pressure struts. The properties of the pressure struts were determined in accordance with FEMA-356 and TBSC-2018 [22, 26].

Table 1 Flexural joint damage limit criteria

Point	Concrete Strain	Steel Strain
B	Determined by yield strength and flexural rigidity	
IO	(ε_c) =0.0035	(ε_s) = 0.01
LS	(ε_{cc})= 0.0035+0. 010·(ρ_c/ρ_s) ≤0.0135	(ε_s)= 0.04
CP	(ε_{cc})= 0.0040+0.014·(ρ_c/ρ_s) ≤0.0180	(ε_s)= 0.06
C-D	(ε_{cc})= 0.03	(ε_s)= 0.5·ε_{su}
E	(ε_{cc})= 0.04	(ε_s)= ε_{su}

In Table 1; ε_c: concrete strain, ε_{cu}: strain at the most outer fiber of concrete, ε_{cc}: strain at the most outer core fiber of the concrete, ρ_s: volumetric ratio of lateral reinforcement present, ρ_c: volumetric ratio of lateral reinforcement required by code, ε_s: reinforcing steel strain, ε_{su}: reinforcing steel ultimate strain value.

3. Determination of nonlinear displacement demands

The buildings modeled in 3-D were subjected to non-linear static analysis considering the vertical load effects and capacity curves were obtained. For 96 models, displacement capacity values at Immediate Occupancy, Life Safety and Collapse Prevention performance levels were obtained according to 2018 Earthquake Regulation. The capacity curves of 3-D models were reduced to "Single Degree of Freedom" (SDOF) models using bi-linearization. Nonlinear displacement demands of the SDOF models were calculated by nonlinear time domain analysis using 264 real earthquake records with different maximum ground acceleration values [27]. The obtained building displacement capacities were compared with the displacement demands. A total of 264 ground motion records were used to calculate the nonlinear displacement demands. All earthquake records were obtained from PEER website [28]. The maximum ground acceleration values of the earthquakes and acceleration records used in the analysis are given in Table 2.

Table 2. The seismic events and the PGA values of the records considered in the study

No	Earthquake	# records	PGA Range (g)
1	Cape Mendocino 1992/04/25 18:06	4	0.385-0.662
2	Chi-Chi, Taiwan 1999/09/20	56	0.119-0.655
3	Coalinga 1983/05/02 23:42	4	0.227-0.592
4	Coyote Lake 1979/08/06 17:05	3	0.228-0.434
5	Duzce, Turkey 1999/11/12	2	0.348-0.535
6	Erzincan, Turkey 1992/03/13	1	0.496
7	Friuli, Italy 1976/05/06 20:00	1	0.351
8	Gazli, USSR 1976/05/17	1	0.608
9	Imperial Valley 1940/05/19 04:37	2	0.215-0.313
10	Imperial Valley 1979/10/15 23:16	33	0.160-0.704
11	Irpinia, Italy 1980/11/23 19:34	11	0.201-0.602
12	Kobe 1995/01/16 20:46	8	0.212-0.693
13	Kocaeli, Turkey 1999/08/17	17	0.137-0.550
14	Landers 1992/06/28 11:58	4	0.152-0.417
15	Livermore 1980/01/24 19:00	1	0.229
16	Loma Prieta 1989/10/18 00:05	38	0.159-0.701
17	Mammoth Lakes 1980/05/27 14:51	1	0.408
18	Morgan Hill 1984/04/24 21:15	2	0.423-0.711
19	N. Palm Springs 1986/07/08 09:20	7	0.205-0.694
20	Northridge 1994/01/17 12:31	34	0.185-0.657
21	Parkfield 1966/06/28 04:26	5	0.357-0.652
22	San Fernando 1971/02/09 14:00	1	0.324
23	Spitak, Armenia 1988/12/07	1	0.199
24	Superstitn Hills(B) 1987/11/24 13:16	10	0.181-0.682
25	Tabas, Iran 1978/09/16	2	0.328-0.406
26	Victoria, Mexico 1980/06/09 03:28	2	0.587-0.621
27	Westmorland 1981/04/26 12:09	7	0.155-0.651
28	Whittier Narrows 1987/10/01 14:42	5	0.199-0.426
29	Whittier Narrows 1987/10/04 10:59	1	0.374
	Total	264	

While comparing earthquake displacement demands and building displacement capacities, earthquake records were divided into 3 groups to reflect the 3 earthquake intensity levels (0.2g, 0.4g and 0.6g) in the seismic codes. The average ground acceleration values of the records with peak ground acceleration values around 0.2g, 0.4g and 0.6g values were divided into 3 groups to reflect these values and used in the comparison. These groups can be considered as ground motions with different return periods. The values related to the acceleration record groups used are given in Table 3. Since there are few acceleration records with high PGA values (0.5g-0.7g) in the literature, fewer acceleration records were used in this group.

Table 3. The acceleration set properties considered in the study

Acceleration Set	Quantity	Min. (g)	Max. (g)	Avg. (g)
0.2g	93	0.119	0.274	0.200
0.4g	108	0.300	0.506	0.400
0.6g	63	0.500	0.711	0.601

4. Analysis results

To assess the impact of the analyzed parameters, we calculated the exceedance probability for each performance level. This probability represents the likelihood that the structural displacement demand will exceed the capacity associated with a specific performance level for a particular set of acceleration records.

Table 4. Exceedance ratios for different cases

1975 Code		C10s200	C16s200	C10sCode	C16sCode
0.2g/IO	S2	0.105	0.046	0.110	0.059
	S4	0.866	0.801	0.874	0.833
	S7	0.769	0.753	0.772	0.755
0.4g/LS	S2	0.009	0.000	0.005	0.000
	S4	0.465	0.218	0.343	0.141
	S7	0.428	0.146	0.118	0.014
0.6g/CP	S2	0.067	0.008	0.036	0.000
	S4	0.746	0.500	0.647	0.393
	S7	0.512	0.258	0.194	0.071
1998 Code		C16s200	C25s200	C16sCode	C25sCode
0.2g/IO	S2	0.024	0.024	0.027	0.024
	S4	0.374	0.427	0.309	0.239
	S7	0.390	0.446	0.446	0.422
0.4g/LS	S2	0.000	0.000	0.000	0.000
	S4	0.005	0.002	0.000	0.000
	S7	0.046	0.000	0.000	0.000
0.6g/CP	S2	0.000	0.000	0.000	0.000
	S4	0.135	0.048	0.000	0.000
	S7	0.163	0.016	0.000	0.000

For the correspondence of performance level and acceleration group, the performance requirements commonly considered for residential buildings was used. According to this, residential structures should have low damage for frequent ground motions (Immediate Occupancy for earthquakes with an average PGA of 0.2g); meet life safety requirements for the design earthquake load (Life Safety for earthquakes with an average PGA of 0.4g). For rare ground motions, total collapse should be prevented (Pre-Collapse for earthquakes with an average PGA of 0.6g). These values are given in Table 4 according to the number of storeys for different structural case, performance levels and code. “S2”, ‘S4’ and ‘S7’ in the

tables indicate the number of stories as 2, 4 and 7. The value after "C" indicates the concrete strength in MPa and the "200" after "s" indicates that the lateral reinforcement spacing is 200 mm. In this case, it is assumed that there are no stirrups in the section. The expression "sCode" indicates that the lateral reinforcement case is in compliance with the relevant code. Under the "Ratio" column, the exceedance ratio of the case in question is given.

5. Results and discussion

When the obtained results are analyzed, following conclusions may be drawn: The exceedance ratio of the Immediate Occupancy performance level is much less affected by changes in concrete strength, lateral reinforcement quantity and detailing when compared to the other performance levels. This is an expected result since this level is at the beginning of the nonlinear behavior. Since concrete strength and amount of lateral reinforcement are more effective on deformation capacity rather than strength, they are not effective on IO, which is mostly determined by strength.

For Immediate Occupancy performance levels, increasing concrete strength and lateral reinforcement can paradoxically lead to higher exceedance rates in certain cases. This occurs because these improvements result in higher longitudinal reinforcement elongation at lower curvature values, while also requiring more lateral reinforcement due to increased concrete strength (as per code regulations). This effect is particularly pronounced in low-rise buildings, where the ductility of beam and column sections is highly sensitive to longitudinal reinforcement elongation. Similar observations have been reported in previous research [29].

For both code cases and all performance levels, the damage rate increases rapidly as the number of storeys increases. It has been observed in many previous studies and post-earthquake investigations that the seismic performance of low-rise buildings is better than high-rise buildings [30–32]

For the 1975 code models, it is seen that 4-storey buildings have a greater risk than 7-storey buildings. One of the reasons for this situation is that 4-storey 1975 code buildings have relatively weaker structural systems. These buildings are partially constructed in a poorer manner due to their low number of storeys due to construction culture in Turkey [20]. In addition, the period values of these structures have values closer to the dominant period of the acceleration records. It is stated that the relative (not absolute) drift demands of these buildings are higher than those of 7-story buildings [33]. For the 1998 code models, it is seen that the increase in the number of storeys and the increase in the damage ratio are parallel.

It is observed that the 1975 code models have significantly high damage ratios for all performance cases. For 2 and 7 storey buildings, low damage ratios are obtained only for LS and CP when both concrete strength and lateral reinforcement amount are positive. These ratios increase significantly with the decrease of material and/or lateral reinforcement properties. Considering that the models used in the study do not have any irregularities, the high exceedance ratios become more striking.

For the 1998 code models, the exceedance ratios are at very low levels. Especially for LS and CP cases, zero or near zero values are obtained unless both concrete strength and lateral reinforcement amount are low. This can be considered as an indication that the 1998 code models have superior seismic performance. Despite the unfavorable concrete strength and lateral reinforcement values, the low exceedance rates can be attributed to the fact that the models do not contain irregularities and the unfavorable concrete strength value is chosen at a value that is not too low such as C16. When the displacement demands

of these models were examined, it was also determined that in most cases the demand values were very close to the capacity values.

It is determined that the IO performance level exceedance rates are high in both regulations, except for 2-storey buildings. Although the 1998 code values are more favorable than the 1975 code, the exceedance rates in the range of 24-45% can be considered high. The effect of concrete strength and lateral reinforcement detailing on the damage rate generally increases as the performance level and the number of storeys increase and is greater for the 1975 code models with lower strength than for the 1998 code models. As an expected result, the effect of material and detailing properties on the performance increases with the increase in the nonlinear displacement demand of the structures.

Concrete strength and lateral reinforcement detailing have a significant effect on the damage rate. For example, for the 1975 code models, for 0.4g/LS, the damage rate of 4-storey models decreases from 47% to 14% and for 7-storey models from 43% to 1%. For 0.6g/CP, there are reductions from 75% to 39% for 4-story models and from 51% to 14% for 7-story models.

In the 1998 code models, the exceedance rates for most of the performance levels other than IO are zero or close to zero, making it more difficult to evaluate. However, in 4 and 7 storey models, the values decrease rapidly between C16s200 and C16sCode ratios and reach zero for other cases, indicating that concrete strength and lateral reinforcement detailing are effective on the damage rate.

6. Conclusions

This study investigates the seismic behavior of reinforced concrete buildings, specifically focusing on the effects of concrete strength and lateral reinforcement detailing. A total of 48 nonlinear inelastic models representing 2-, 4-, and 7-storey residential buildings were analyzed using both static and dynamic methods. The capacity curves were derived through linear inelastic static analysis, and displacement demands were calculated using nonlinear inelastic time domain analysis across 264 acceleration records. The study aimed to assess how variations in concrete strength and lateral reinforcement influence the exceedance rates of different performance levels, particularly Immediate Occupancy (IO), Life Safety (LS), and Collapse Prevention (CP).

- The exceedance ratio for the IO performance level is minimally affected by changes in concrete strength and lateral reinforcement, as IO is primarily governed by strength rather than deformation capacity.
- Paradoxically, increasing concrete strength and lateral reinforcement can lead to higher IO exceedance rates in low-rise buildings. This is attributed to increased longitudinal reinforcement elongation at lower curvature values, necessitating additional lateral reinforcement.
- Damage rates increase with the number of storeys, with low-rise buildings generally exhibiting better seismic performance than high-rise structures.
- For the 1975 code models, 4-storey buildings showed higher exceedance rates than 7-storey buildings due to weaker structural systems, higher relative drift demands, and construction practices.
- The 1998 code models showed superior seismic performance, with near-zero exceedance rates for LS and CP under most conditions, even with low concrete strength.

- High exceedance ratios for the 1975 code models highlight the significance of modern seismic design practices and improved detailing requirements.
- At CP performance levels under high-intensity ground motion (0.6g), significant reductions in exceedance rates were observed when transitioning from inadequate to code-compliant detailing emphasizing the effect of considered parameters in highly nonlinear behavior.
- Concrete strength and lateral reinforcement detailing are crucial for improving seismic performance, particularly for older code models. Their impact becomes more pronounced at higher performance levels (LS and CP) and for taller buildings.

This study highlights the critical influence of material properties, lateral reinforcement detailing, and building height on the seismic performance of RC structures. While modern seismic design codes have significantly improved performance outcomes, older code-compliant buildings remain vulnerable under higher seismic demands. The findings emphasize the need for retrofitting strategies and stricter enforcement of seismic design standards to ensure the resilience and safety of the built environment.

Acknowledgement

This study was supported by TUBITAK Scientific Research Project No. 107M569.

References

[1] Işık E, Hadzima-Nyarko M, Bilgin H, Ademović N, Büyüksaraç A, Harirchian E, et al. A Comparative Study of the Effects of Earthquakes in Different Countries on Target Displacement in Mid-Rise Regular RC Structures. Appl Sci. 2022; 12(23).

[2] Chen X, Fu J, Hao X, Yang H, Zhang D. Seismic behavior of reinforced concrete squat walls with high strength reinforcements: An experimental study. Struct Concr. 2019; 20(3):911–31.

[3] Ozmen HB, Tarakci NG. Effect of soil and foundation stiffness on the seismic behavior of mid-rise RC buildings. Res Eng Struct Mater. 2022; 8(2).

[4] Shin J, Scott DW, Stewart LK, Yang C-S, Wright TR, DesRoches R. Dynamic response of a full-scale reinforced concrete building frame retrofitted with FRP column jackets. Eng Struct. 2016; 125:244–53.

[5] Choi M-H, Lee C-H. Seismic Behavior of Existing Reinforced Concrete Columns with Non-Seismic Details under Low Axial Loads. Materials (Basel). 2022; 15(3):1239.

[6] Işık E. Investigation of the contribution of the reinforcement tie to the seismic behavior of reinforced-concrete columns. Bitlis Eren Univ J Sci Technol. 2022; 12(1):21–6.

[7] Yuksel SB, Foroughi S. Betonarme Dairesel Kolonların Eğilme Momenti-Eğrilik ve Hasar Sınırlarının Analizi. Eur J Sci Technol. 2020;(19):891–903.

[8] Deng M, Zhang Y. Seismic Performance of High-Ductile Fiber-Reinforced Concrete Short Columns. Mander J, editor. Adv Civ Eng. 2018; 2018(1).

[9] Chen SW, Yang M, Hou ZX, Li GQ, Liu Q. Experimental and Numerical Studies on Seismic Behavior of Q460 High Strength Steel Reinforced Concrete Column. Key Eng Mater. 2018; 763:763–70.

[10] Han SW, Kang JW, Lee CS. Seismic Behavior of Slender HPFRCC Coupling Beams with Limited Transverse Bars. Earthq Spectra. 2018; 34(1):77–98.

[11] Dang H V, Lee K, Han SW, Kim SJ. Experimental assessment of the effects of biaxial bending moment and axial force on reinforced concrete corner columns. Struct Concr. 2018; 19(4):1063–78.

[12] Foroughi S, Yuksel SB. Investigation of The Moment–Curvature Relationship for Reinforced Concrete Square Columns. Turkish J Eng. 2020; 4(1):36–46.

[13] Zhang HM, Lu XL, Duan YF, Zhu Y. Experimental Study on Failure Mechanism of RC Walls with Different Boundary Elements under Vertical and Lateral Loads. Adv Struct Eng. 2014; 17(3):361–79.

[14] Cansız S. Effect of tightening zone length of reinforced concrete beams on beam capacity.

Gradjevinar. 2022; 74(10):857–68.
[15] Cruze D, Sah C, Manikanta N, Mandal DK, Jha AK, Solomon AA. Axial compressive behavior of recycled aggregate concrete steel composite columns. Res Eng Struct Mater. 2024; 10(3):1155–71.
[16] Lim H-K, Kang J, Pak H, Chi H-S, Lee Y, Kim J. Seismic Response of a Three-Dimensional Asymmetric Multi-Storey Reinforced Concrete Structure. Appl Sci. 2018; 8(4):479.
[17] Moon D-S, Lee Y-J, Lee S. Fragility Analysis of Space Reinforced Concrete Frame Structures with Structural Irregularity in Plan. J Struct Eng. 2018; 144(8).
[18] Turkish Earthquake Code-TEC (1975): Specifications for structures to be built in seismic areas. Ankara, Turkey; 1975.
[19] Turkish Earthquake Code-TEC (1998): Specifications for structures to be built in seismic areas. 1998.
[20] Ozmen HB, Inel M, Senel SM, Kayhan AH. Load carrying system characteristics of existing turkish rc building stock. Int J Civ Eng. 2015; 13(1).
[21] SAP2000. Integrated Software for Structural Analysis and Design. Berkeley, USA: Computers and Structures Inc.; 2024.
[22] TBSC. Turkish Building Seismic Code. Ministry of Environment and Urban Planning, Ankara, Turkey; 2018.
[23] Modeling Non-Linear Behavior of Reinforced Concrete Members, TUBITAK, 105M024, 2005-2008.
[24] Mander JB, Priestley MJN, Park R. Theoretical Stress-Strain Model for Confined Concrete. J Struct Eng. 1988; 114(8).
[25] TS-500: Requirements for design and construction of reinforced concrete structures. Turkish Standards Institute, Ankara, Turkey; 2000.
[26] FEMA-356. Prestandard and commentary for the seismic rehabilitation of buildings, Federal Emergency Management Agency. American Society of Civil Engineers (ASCE), Washington, DC, USA. Washington, USA; 2000.
[27] HACHEM MM. BiSpec [Internet]. 2016.
[28] PEER. Pacific Earthquake Engineering Research Center [Internet]. Available from: http://peer.berkeley.edu/smcat/index.html
[29] Ozmen HB. Düşük ve orta yükseklikteki betonarme yapıların deprem performanslarını etkileyen faktörlerin irdelenmesi. Dissertation. Pamukkale University- Graduate School of Natural and Applied Science; 2011.
[30] Ozmen HB, Inel M. Strength reduction factors for existing mid-rise RC buildings for different performance levels. Res Eng Struct Mater. 2018; 4(4):241–55.
[31] Ozmen HB, Inel M, Cayci BT. Engineering implications of the RC building damages after 2011 Van Earthquakes. Earthquakes Struct. 2013; 5(3):297–319.
[32] Ozmen HB, Inel M, Demirtas Y. Evaluation of different cases of soft story formation for mid-rise RC buildings. Res Eng Struct Mater. 2020; 6(3).
[33] Inel M, Ozmen HB, Onur O, Celik S. Nonlinear seismic displacement demands of mid-rise reinforced concrete buildings subjected to past earthquakes in Turkey. In: 9th International Congress on Advances in Civil Engineering. Trabzon, Turkey; 2010. p. Paper ID: SEE-131.

MIM Research Group Research & Design
www.jrede.org

Review Article

Exploring the potential of natural zeolites to enhance solar energy systems: A concise review

Canan Kandilli*[a]

Department of Mechanical Engineering, Usak University, Türkiye.

Article Info

Article History:

Received: 1 Nov 2024

Accepted: 30 Nov 2024

Keywords:

Sensible heat storage materials;

Solar energy systems;

Natural zeolites;

Key parameters;

Innovative solar applications

Abstract

When examining the initial applications of natural zeolites for solar energy in recent history, it becomes apparent that homes in hot climates are often constructed with very thick walls with a high thermal mass. These walls absorb heat during the day and release it at night, maintaining a cooler indoor environment throughout the day. In countries like Turkey and Italy, where zeolitic tuff deposits are abundant, it is common to find structures with thick walls made from this natural stone. This study aims to explore the potential of natural zeolites for enhancing solar energy systems. The general properties of natural zeolites are examined, and topics such as the history of natural zeolites, reserves and consumption, application areas, and the thermo-physical properties of these materials are discussed. Existing solar energy systems utilizing natural zeolites have been reviewed, while innovative solar applications for both residential and industrial settings are proposed. It is hoped that this study will offer a multidisciplinary perspective for researchers and practitioners alike contribute the design solutions for such systems.

1. Introduction

Solar energy has an intermittent and irregular nature throughout the day, with its availability fluctuating based on time of day, season, and weather. Consequently, it is essential to develop effective storage methods to harness solar energy obtained during sunlight hours for use at other times, thereby ensuring a longer-lasting and stable thermal output from solar energy systems. Natural zeolites, of which over 40 naturally occurring frameworks are known, are industrially produced and widely used for many products across various sectors [1].

Although natural zeolites are already utilized in many areas, further research into their various types and properties could transform them into high-value products with additional applications in existing systems. This study presents an overview of the general and thermophysical properties of natural zeolites and their potential applications in design of solar energy systems, as well as recent research conducted in this area. For the first time in the literature, innovative solar energy systems utilizing the sensible heat storage capacity of natural zeolites are introduced.

*Corresponding author canan.kandilli@usak.edu.tr
[a]orcid.org/ 0000-0001-7159-4174
DOI: http://dx.doi.org/10.17515/rede2024.001en1101rv
Res. Des. Vol. 1 Iss. 1 (2024) 13-21

2. General Properties of Natural Zeolites

2.1. History of Natural Zeolites

The term 'zeolite' was first introduced in 1756 by Swedish mineralogist Axel Fredrik Cronstedt, who named it 'boiling stone' due to its ability to produce steam when it acts as an adsorbent [2]. The utility of zeolites began to be recognized in research by chemists Weigel and Steinhoff nearly two centuries after the discovery of the first zeolite mineral. They found that evaporated zeolites could adsorb small organic molecules but did not accommodate larger ones. In 1932, McBain coined the term 'molecular sieve' for zeolites due to their capacity to separate molecules based on size. Research between 1940 and 1945 further highlighted their industrial and commercial importance, particularly due to their adsorption and gas separation capabilities. In 1948, Milton and colleagues synthesized the first synthetic zeolite crystal, known as Linda A, and today over 400 synthetic zeolites exist. Zeolites, a group of over 40 naturally occurring microporous aluminosilicate minerals, are widely utilized as adsorbents, catalysts, and in various industrial applications. Of these, 14 types hold particular industrial significance and are commonly used. The most prevalent natural zeolite minerals include phillipsite, chabazite, heulandite, laumontite, natrolite, stilbite, erionite, and clinoptilolite. Since 1977, the International Zeolite Association (IZA) has been compiling and preparing zeolite structural data for scientific use [3].

Looking at historical solar energy applications, we observe that homes in hot climates are often constructed with thick walls with high thermal mass, which store heat during the day, releasing it at night to maintain cool temperatures indoors. In countries like Turkey and Italy, where zeolitic tuffs are abundant, it is common to encounter structures with thick walls made from this natural stone.

2.2 Natural Zeolite Reserve and Consumption

There are no reliable data on the estimation of natural zeolite reserves for the whole world. Although zeolite is mined in many countries, most of these reserves are of low or medium concentration volcanic tuffs. According to the U.S. Geological Survey, Mineral Commodity Summaries report published in January 2020, reserve estimates should be adjusted according to these concentration ratios. Although it varies according to the zeolite percentage, chemical and physical properties, particle size, surface modification and/or activation, the average zeolite sales price is stated in this report as $125 per ton [4].

According to this report, two leading mining companies in America stated that their total zeolite reserves were 80 million tons. However, although it is known that the reserves are very abundant throughout the world, exact figures are not available. In the Fig.1, zeolite mineral production values by countries were presented. When we look at the zeolite deposits in Turkey, zeolite deposits are rich in regions such as Balıkesir - Bigadiç, Manisa - Gördes, İzmir - Urla, Kütahya - Şaphane and Cappadocia. Clinoptilolite, chabazite, mordenite, erionite and analcime minerals are mostly concentrated in these deposits. Clinoptilolite is the most sought-after zeolite mineral in the world, and today it accounts for 80% of mining in Gördes (Manisa) and Bigadiç (Balıkesir) regions [5]. In 2001, upon a question directive given to the Turkish Grand National Assembly regarding zeolite reserves, it was stated that the existence of zeolite reserves in Turkey was understood in 1971, only Bigadiç among the zeolite deposits was investigated, and there were 500 million tons of zeolite reserves that could be processed here. In addition, together with these reserves, the answer was presented that Turkey's possible total zeolite reserves are estimated to exceed 50 billion tons. [6]. Although the exact values are not known, it is stated that 62% of the natural zeolite reserves in the world are in Turkey [7]. Despite the large

reserves, the necessity of producing high value-added products that can be imported has been expressed for many years.

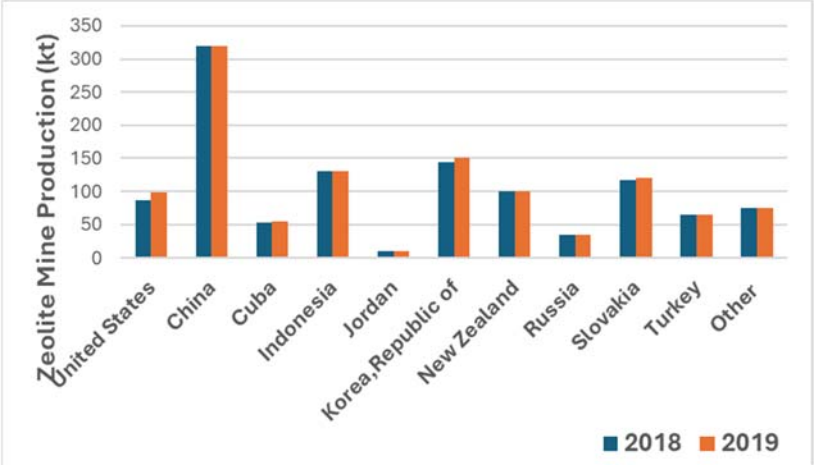

Fig. 1. Zeolite mineral production for the years 2018 and 2019 by countries [Data were adopted the U.S. Geological Survey, Mineral Commodity Summaries report, 2020]

2.3 Usage Areas of Natural Zeolites

The main physical and chemical properties of eoliths are; The ability to exchange ions, adsorption and the resulting molecular sieve structure, silica content, as well as the light color, lightness and pore structure of small crystals in sedimentary zeolites have led to the use of zeolites in a wide variety of industrial areas. The areas of use where one or more of these properties of natural zeolites, which have become an important industrial raw material in recent years, are required can be grouped into 5 main sections: pollution control, energy, agriculture-livestock, mining-metallurgy and other fields. In Table 1, usage areas and natural zeolites types are reported [8].

Table 1. Usage areas and zeolite types

Area	Materials for which zeolite can be used as a substitute
Animal husbandry	Bentonite, sepiolite, dolomite, gypsum, iodine, iron oxide, limestone, magnesite, manganese, perlite, phosphates, salt, sulfur, talc, vermiculite
Ion carrier	Attapulgite / sepiolite, bentonite, diatomite, kaolin, pumice, pyrophyllite, talc, vermiculite
Detergent production	Sodium tripolyphosphate, sodium silicate, citrate
Lightweight aggregate	Clays, perlite, pumice, shale, vermiculite
Molecular Sieve	Activated carbon, activated clays, powdered alumina, attapulgite / sepiolite, bentonite, silica gel
Animal Litter	Diatomite, attapulgite / sepiolite, bentonite, kaolin
Radioactive Waste, Cleaning of Waste Water, Cleaning of Flue Gases, Cleaning of Oil Spills	Clinoptilolite and mordenite

3. Thermo-Physical Properties of Natural Zeolites

When we consider them as sensible heat storage materials, the most basic thermo-physical properties of natural zeolites are density, thermal conductivity and specific heat. In Table2, Table3 and Table 4, thermal conductivity, density, specific heat and some descriptive structural features of natural zeolites are presented [9,10]. From Table 2, as particle size increases from Z1 to Z3, both thermal conductivity and density decrease. Plate forms show higher thermal conductivity and lower density compared to particle forms, indicating potential for applications requiring enhanced thermal conductivity and reduced weight. Plate forms display significantly higher thermal conductivity compared to particle forms, with values between 0.514 W/m·K and 0.550 W/m·K, increasing slightly from Z1 to Z3. Table 3 provides data on the thermal conductivity and specific heat of three different zeolite samples (Z1, Z2, Z3) across a temperature range from 30°C to 100°C. Thermal conductivity decreases with increasing temperature for all samples. Z1 has the highest thermal conductivity values, ranging from 0.187 W/m·K at 30°C to 0.151 W/m·K at 100°C. Z2 has intermediate values, starting at 0.142 W/m·K at 30°C and dropping to 0.096 W/m·K at 100°C. Z3 has the lowest thermal conductivity, decreasing from 0.124 W/m·K at 30°C to 0.083 W/m·K at 100°C. On the other hand, specific heat generally increases with temperature across all samples, though there are minor fluctuations. Z1 starts with a specific heat of 410 J/kg·K at 30°C and reaches a peak of 1810 J/kg·K at 80°C, then declines slightly at higher temperatures. Z2 shows a consistent increase in specific heat, from 1140 J/kg·K at 30°C to a peak of 2980 J/kg·K at 80°C, then decreases at higher temperatures. Z3 follows a similar trend, with specific heat increasing from 1100 J/kg·K at 30°C to 3030 J/kg·K at 80°C, before slightly reducing at higher temperatures. Some detailed structural properties are given in Table 4 for Gördes clinoptilolite [11].

Table 2. Thermal conductivity and density with particle size and plate form

Particle size (mm)	Thermal conductivity (W/mK)	Density (kg/m3)
0.1-1 (Z1)	0.150	1905
1.0-3.0 (Z2)	0.134	1780
4.0-5.0 (Z3)	0.099	1667
Plate form Z1	0.514	1503
Plate form Z2	0.549	1470
Plate form Z3	0.550	1428

4. Proposed Designs of Novel Solar Energy Systems with Natural Zeolites

In many studies in the past, both natural and synthetic zeolites have been used as a type of heat exchanger in heat pumps thanks to their adsorption properties [12]. However, this study focuses on systems developed by taking advantage of the sensible heat storage properties of natural zeolites. Considering the use of natural zeolites with solar energy, they have the potential to be an important component in establishing a structure that will provide more stable and stable storage of solar energy and retain heat, thanks to their heat storage properties.

Table 3. Thermal conductivity and specific heat with temperature

Temperature (°C)	Thermal conductivity (W/mK)			Specific heat (J/kgK)		
	Z1	Z2	Z3	Z1	Z2	Z3
30	0.187	0.142	0.124	410	1140	1100
40	0.172	0.131	0.119	520	1390	1520
50	0.164	0.124	0.114	1260	1930	2010
60	0.161	0.119	0.102	1540	2650	2450
70	0.158	0.11	0.106	1660	2950	2800
80	0.154	0.102	0.098	1810	2980	3030
90	0.151	0.108	0.092	1670	2870	3010
100	0.151	0.096	0.083	1490	2670	2830

Table 4. Structural features of Gördes clinoptilolite [11]

Parameter	Value
Chemical formula	(Na0.5K2.5)(Ca1.0Mg0.5)(Al6Si30)O72.24H2O
Mineralogical composition of the raw material	Clinoptilolite (%85-90) + Smectite(%5-6), Opal-CT(5-6)+Quartz(<3)
Clinoptilolite identification	Rich in potassium, potassium, calcium, clinoptilolite
Color	Natural rock; white, beige, light beige, almond green
Toughness (Mohs)	3
Bulk density	500-1200 kg/cm^3 (depending on grain sizes ranging from powder to < 15 mm)
Volumetric weight (dry)	1.4-1.7 g/cm^3
Volumetric weight (saturated)	1.8-2.0 g/cm^3
Specific weight	2.1 g/cm^3
Visible porosity	35%
Water adsorption capacity	135%
Resistance to acid, base environment (pH):	2.0-12.0
Surface area	40.79 m^2/g
Thermal resistance	up to 750 °C
Pressure Strength	10.10 MPa
Clinoptilolite crystal size	5-15 µm
Average pore radius	0.041 µm
Water absorption by weight	23%
Ammonium (NH4) ion exchange capacity	1.6-2.0 meq/g
CO2 adsorption	94 mg CO_2/g

According to IS0 and CEN standards, materials with a thermal conductivity coefficient of less than 0.065 W/mK are defined as thermal insulation materials and are the most decisive feature in the selection of thermal insulation materials. Ozcelik (2010)

investigated physical and mechanical properties of foam materials which are obtained by using natural clinoptilolite samples and foaming materials. It was observed that the clinoptilolite samples also formed a porous structure at 1300 °C. It has been revealed that the thermal conductivity coefficients of the majority of SiC-containing foam materials are much lower than 0.065 W/mK (up to 0.029 W/mK) [13]. In this section, in the light of these thermophysical properties, the application and potential improvements of natural zeolites to known solar energy systems will be discussed.

4.1 Solar Thermal Collectors Enhanced with Natural Zeolites (STC-NZ)

Structure of solar thermal collector improved by natural zeolite plates is given by Fig.2. In the framework of an ongoing project [14], a conventional solar thermal collector has been improved by natural zeolite plates and some experiments have been conducted. As known, output temperature of a STC changes by incoming solar radiation. It is possible to obtain the thermal energy from this system at a more constant temperature, to balance temperature changes during the day and to continue obtaining thermal energy after sunset, thanks to the heat storage feature of natural zeolites. The qualitative results of this project will be the subject of another study.

Fig. 2. Structure of STC-NZ [14]

4.2 Photovoltaic thermal (PVT) system enhanced with natural zeolites (PVT-NZ)

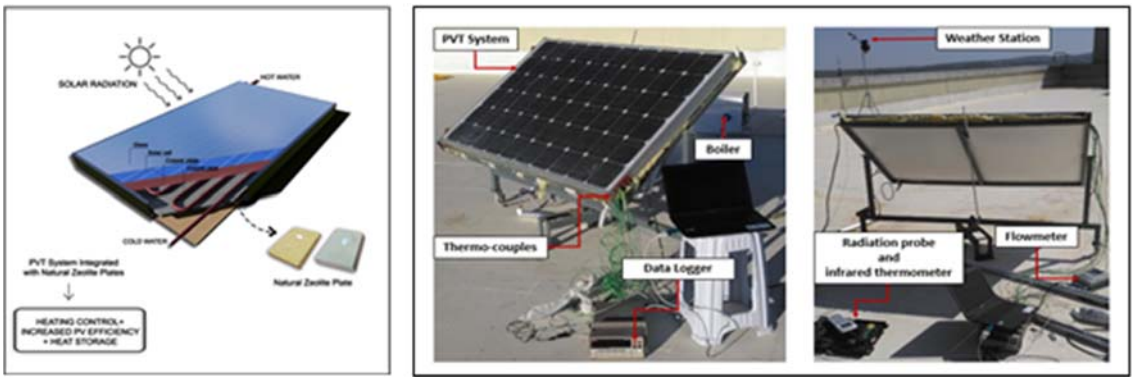

Fig. 3. Structure and test system of PVT-NZ [15]

Structure and test system of PVT-NZ present by Fig. 3. In photovoltaic panels, solar radiation that cannot be converted into electricity causes overheating. This excess heat can be removed from the PV back surface with different fluids in PVT systems. This heat can be used as thermal energy. In PVT systems, both phase change materials containing latent heat and sensible heat storage materials can be used. Thus, the waste heat generated during electrical conversion is removed, ensuring that the electrical efficiency of the PV

panel does not decrease, and this heat can also be used as a thermal energy source. Natural zeolite plates enable waste heat to be absorbed and used as thermal energy in PVT systems. The performance of PVT systems integrated with natural zeolite plates increases with their porous structure and high heat storage properties [15,16]. In the experiments, thermal efficiency of up to 69% and leaving water temperatures of 53.4 °C were achieved. For the proposed system, the payback period is calculated as 1.99 years for industrial applications and 3.76 years for residence tariff. Detailed qualitative results of the experiments will be presented as a result of another study.

4.3 Natural Zeolites for Nearly Zero Energy Building (nZEB) Applications

In general, near-zero energy buildings (nSEB) are considered highly energy efficient buildings powered by renewable energy to compensate for the energy demand. The concept is taken from the European Parliament Energy Performance of Buildings Directive (EPBD) [Directive (EU) 2010/31/EU]. The directive stipulates that buildings constructed after 31 December 2020 and that need to be heated or cooled according to their purpose must be built as nSEB. Trombe wall systems, one of the passive solar energy techniques, are low-cost, high-efficiency systems that have been known for many years and can be applied to existing buildings. The energy heated and stored by solar radiation throughout the day heats the indoor air and the interior is naturally heated thanks to the natural circulation that occurs. Thanks to the high heat storage capacity of natural zeolites, the stored energy will continue to provide thermal energy to the environment at the end of the day. The effectiveness of Trombe walls has the potential to be increased by using natural zeolite composite plates as thermal mass. In Fig. 4, prototype test room of Composite Trombe Wall (CTW) studied in ongoing project is given. In this study, Perlite was added to natural zeolite to reduce thermal conductivity. Natural zeolite-perlite composite plates low thermal conductivity (about 0.10 W/mK) and high heat capacity (about 5.29x106 J/m3K) can be used in the construction sector as a building material with their low-cost superiority. It can be used as a heat storage material within the scope of zero energy buildings. It will ensure that passive solar energy systems become widespread in the Renewable Energy systems sector. CTW offers the Trombe wall system as a strong option within the scope of nSEB, with its applicability to existing buildings, offering a wide range of architectural options, being usable in every climate zone, low cost and high efficiency potential, especially in heating.

Fig. 4. Test system of Composite Trombe Wall [17]

In general, near-zero energy buildings (nSEB) are considered highly energy efficient buildings powered by renewable energy to compensate for the energy demand. The concept is taken from the European Parliament Energy Performance of Buildings Directive

(EPBD) [Directive (EU) 2010/31/EU]. The directive stipulates that buildings constructed after 31 December 2020 and that need to be heated or cooled according to their purpose must be built as nSEB. Trombe wall systems, one of the passive solar energy techniques, are low-cost, high-efficiency systems that have been known for many years and can be applied to existing buildings. The energy heated and stored by solar radiation throughout the day heats the indoor air and the interior is naturally heated thanks to the natural circulation that occurs. Thanks to the high heat storage capacity of natural zeolites, the stored energy will continue to provide thermal energy to the environment at the end of the day. The effectiveness of Trombe walls has the potential to be increased by using natural zeolite composite plates as thermal mass. In Fig.4, prototype test room of Composite Trombe Wall (CTW) studied in ongoing project is given. In this study, Perlite was added to natural zeolite to reduce thermal conductivity. Natural zeolite-perlite composite plates low thermal conductivity (about 0.10 W/mK) and high heat capacity (about 5.29x106 J/m3K) can be used in the construction sector as a building material with their low-cost superiority. It can be used as a heat storage material within the scope of zero energy buildings. It will ensure that passive solar energy systems become widespread in the Renewable Energy systems sector. CTW offers the Trombe wall system as a strong option within the scope of nSEB, with its applicability to existing buildings, offering a wide range of architectural options, being usable in every climate zone, low cost and high efficiency potential, especially in heating.

5. Conclusions

It is important to transform natural resources into high value-added and economical products in different areas. Disadvantages of solar energy systems, which are the leading renewable energy source, such as storage and intermittency, can be minimized with sensible heat storage materials. In this study, general and thermophysical properties of natural zeolites and effective system suggestions for improving solar energy systems are put forward. Due to reasons such as the difficulty of application of phase change materials, their cost and limited lifespan due to the charge-discharge cycle, the potential of using natural zeolites, one of the sensible heat storage materials, in solar energy systems attracts attention. Some significant indications made in this study are given below:

- The usage areas of natural zeolites can be expanded as sensible heat storage materials.
- By making different additives to natural zeolites, their thermophysical properties can be made suitable for use in solar energy systems.
- Natural zeolite composite plates have a significant potential in obtaining regular and stable thermal energy in solar energy systems.
- Low-cost composite natural zeolite plates can be used to improve performance in STC, PVT and Trombe wall systems.
- It may be possible to use composite natural zeolite plates as a sensible heat storage material in every climate and geography, as an alternative to phase change materials.

Natural zeolites will certainly have potential and new applications that are expected to be discovered, which cannot be listed here. Transforming low-cost and abundant raw materials into high added value products and increasing the efficiency of solar energy systems will make significant contributions to the spread of renewable systems and sustainability.

Acknowledgement

This present work was developed within the framework of research projects which have project number BAP-2023/LP003, 5180034 and 122M882 and fully funded by The Scientific and Technological Research Council of Turkey (TUBITAK). The author would like to thank TUBITAK for the financial support given to the projects.

References

[1] Database of Zeolite Structures [Internet]. International Zeolite Association; 2017 [cited 2021 May 24]. Available from: http://www.iza-structure.org/
[2] Wikipedia. Zeolite [Internet]. [cited 2024 Mar 24]. Available from: https://en.wikipedia.org/wiki/Zeolite
[3] International Zeolite Association [Internet]. [cited 2021 Jun 25]. Available from: http://www.iza-structure.org/
[4] U.S. Geological Survey. Mineral commodity summaries 2020: Zeolites [Internet]. [cited 2021 Jun 25]. Available from: https://pubs.usgs.gov/periodicals/mcs2020/mcs2020-zeolites.pdf
[5] Bilgin Ö, Kantarcı S. Bigadiç (Balıkesir, Türkiye) civarında gözlenen höylandit/klinoptilolit zeolit oluşumlarının teknolojik özelliklerinin incelenmesi. J BAUN Inst Sci Technol. 2018;20(1):589-601. doi: 10.25092/baunfbed.429367.
[6] Türkiye Büyük Millet Meclisi. Tutanak Dökümanları [Internet]. [cited 2021 Jun 25]. Available from: https://www.tbmm.gov.tr/tutanaklar/TUTANAK/TBMM/d21/c073/b011/tbmm2107301103 12.pdf
[7] MEC Enerji [Internet]. [cited 2021 Jun 25]. Available from: https://www.europages.com.tr/MEC-ENERJI/00000005413287-750240001.html
[8] MTA. Zeolit [Internet]. [cited 2024 Mar 24]. Available from: https://www.mta.gov.tr/v3.0/bilgi-merkezi/zeolit
[9] Kandilli C, Acikbas Y, Uzel M. Thermophysical properties of natural zeolite plates enhanced with aluminum granule for thermal management of photovoltaic thermal systems (PVTs). J Energy Storage. 2022;50:104331.
[10] Kandilli C, Acikbas Y, Uzel M. Investigation of thermophysical properties of natural zeolite plates enhanced with graphite powder for thermal management of PV thermal systems. J Cleaner Prod. 2021;318:128558.
[11] Bilgin Ö. Gördes zeolitlerinin hammaddesel özelliklerinin incelenmesi ve değişik sektörlerde kullanılabilirliğinin araştırılması [PhD thesis]. İzmir: Dokuz Eylül University; 2009.
[12] Solmuş İ, Yamalı C, Kaftanoğlu B, Baker D, Çağlar A. Adsorption properties of a natural zeolite–water pair for use in adsorption cooling cycles. Appl Energy. 2010;87(6):2062-2067.
[13] Özçelik H. Natural zeolite applications in physics [PhD thesis]. Eskişehir Anadolu University Graduate School of Sciences; 2010.
[14] Kandilli C. Experimental determination of natural zeolite plate heat storage system integrated solar thermal collector production and performance. Uşak: Uşak University; 2023. (BAP-2023/LP003).
[15] Kandilli C. Design, production, and optimization of the novel photovoltaic thermal system (PVT) integrated with natural zeolite. TÜBİTAK 1505; 5180034.
[16] Kandilli C. Energy, exergy, and economic analyses of a photovoltaic thermal system integrated with the natural zeolites for heat management. Int J Energy Res. 2019; 43:4670–85.
[17] Kandilli C. Production, performance evaluation, and optimization of natural zeolite plate composite Trombe wall system for nearly zero energy buildings (NSEB). TÜBİTAK 1005.

MIM Research Group Research & Design
www.jrede.org

Research Article

Comparative assessment of seismic analysis procedures: Eurocode 8 vs KTPN2-89

Idlir Frangu[*1], Huseyin Bilgin[2a]

[1]*Elteknik - Project Manager, ION Solutions Albania - CEO, Tirana, Albania.*
[2]*Department of Civil Engineering, Epoka University, Tirana, Albania*

Article Info

Article History:

Received: 4 Dec 2024

Accepted: 2 Dec 2024

Keywords:

Earthquake analysis;

Design spectra;

Analytical modelling;

Eurocode 8;

KTP.N2-89

Abstract

This paper evaluates seismic design considerations for a typical reinforced concrete (RC) building in Albania, comparing the provisions of Eurocode 8 (EC8) and the Albanian seismic code, KTP.N2-89. The primary focus is on the design spectra, analyzing differences in site coefficients, spectral shapes, and the inclusion of near- and far-field seismic concepts in EC8. The study applies both codes to various soil types, calculating base shear demands and highlighting key discrepancies. EC8 introduces detailed soil classification using shear wave velocity (VS-30) and site factors, offering a more nuanced framework compared to KTP.N2-89's simpler system. Base shear demands generally increase with softer soils, with EC8 Type 1 producing the highest values across all soil types due to its more conservative approach. In contrast, KTP.N2-89 often results in lower base shear values, except for very soft soils, where its k_E factor amplifies seismic forces. The findings reveal limitations in KTP.N2-89, particularly its lack of comprehensive guidelines for soil effects and earthquake source characteristics. The study emphasizes the need to revise Albania's seismic code, adopting EC8's advanced methodologies to improve structural resilience and ensure safer designs in earthquake-prone regions.

1. Introduction

Over the past two decades, seismic codes in Europe have undergone substantial revisions, primarily in response to the increasing frequency and severity of destructive earthquakes. This evolution reflects a growing recognition of the need for enhanced resilience in building structures against seismic events. The Albanian seismic code, KTP.N2-89 [1], is also poised for revision, aligning with Eurocode standards to ensure that structures are designed to withstand seismic forces effectively. The transition to Eurocode standards is particularly significant for Albania, a country that has experienced notable seismic events, including the devastating earthquake in November 2019, which highlighted vulnerabilities in existing structures [2-5]. The revisions in seismic codes across Europe, including Albania, are informed by extensive research and analysis of past earthquakes. For instance, studies have shown that the performance-based seismic design (PBSD) approach, which emphasizes the assessment of structural performance under various seismic scenarios, is becoming increasingly prevalent in modern codes, including Eurocode 8 [6]. This shift towards performance-based design is crucial, as it allows for a more nuanced understanding of how structures respond to seismic forces, taking into account factors such as building height, material properties, and architectural irregularities [7]. The

*Corresponding author: idlir.frangu@ionsolutions.al
[a]orcid.org/ 0000-0002-5261-3939
DOI: http://dx.doi.org/10.17515/rede2024.002bu1104rs
Res. Des. Vol. 1 Iss. 1 (2024) 23-32

adoption of such methodologies is essential for ensuring that new constructions are not only compliant with current standards but also resilient to potential future seismic events.

In Albania, the need for a revised seismic code is underscored by the findings of probabilistic seismic hazard assessments, which indicate that many existing buildings do not meet the necessary safety standards [8]. The current KTP.N2-89 code, while a foundational document for seismic design, lacks the comprehensive guidelines found in more contemporary codes like Eurocode 8 [9]. This inadequacy has led to calls for a thorough reassessment of the code, particularly in light of the vulnerabilities exposed during recent earthquakes [2]. The integration of advanced methodologies, such as the N2 method for displacement demand evaluation, is vital for improving the seismic resilience of Albanian structures [10].

The classification of soil types and their associated effects on seismic performance is a critical aspect of structural engineering, particularly in seismic-prone regions. Eurocode 8 provides a framework for understanding these site effects through soil categorization, delineating five primary soil types along with two special categories, each assigned a soil factor "S" that influences seismic design parameters. Conversely, KTP.N2-89 recognizes only three soil types without a corresponding soil factor, which may limit its applicability in nuanced seismic assessments. The classification in Eurocode 8 is grounded in empirical parameters such as mean shear wave velocity, standard penetration tests, unconfined compression tests, and relative density, which are essential for determining soil behavior under seismic loading conditions.

The shear wave velocity (V_S−30) is particularly significant in site classification as it serves as a robust indicator of soil stiffness and, consequently, its seismic response. Research has proposed that V_S−30 can be effectively utilized in building codes to classify sites, thereby enhancing the accuracy of seismic risk assessments. This method aligns with the principles outlined in Eurocode 8, which employs shear wave velocity as a critical parameter in its soil classification system. The incorporation of V_S−30 allows for a more refined understanding of how different soil types will respond during seismic events, thus informing more effective engineering practices.

Table 1. Ground types defined in Eurocode 8 (EC8) and KTP.N2-89

Eurocode 8				KTP.N2-89
Soil Type		Type 1	Type 2	Soil Type
Rock (A)	Vs,30>800 m/s	S=1	S=1	Rock (I)
Firm (B)	360<Vs,30<800 m/s	S=1.2	S=1.35	Stiff (II)
Soft (C)	180<Vs,30<360 m/s	S=1.15	S=1.5	Soft (III)
Very soft (D)	Vs,30< 180 m/s	S=1.35	S=1.8	

Table 1, which details the soil classifications from both Eurocode 8 and KTP.N2-89, illustrates the differences in soil types, shear wave velocities, and the site factor "S" values for both spectra Types 1 and 2 as defined in Eurocode 8. This comparative analysis reveals that Eurocode 8's more detailed classification system, which includes a range of soil factors, may provide a more comprehensive framework for seismic design compared to KTP.N2-89's simpler categorization. The soil factors in Eurocode 8 account for the varying degrees of seismic risk associated with different soil types, thereby facilitating more tailored engineering solutions.

The classification of soil types in Eurocode 8 plays a crucial role in understanding site effects on seismic performance. The detailed categorization in Eurocode 8, which

incorporates shear wave velocity and soil factors, provides a more nuanced approach to seismic design compared to the simpler framework of KTP.N2-89. As the field of geotechnical engineering continues to evolve, the integration of empirical data and advanced classification methodologies will be essential for enhancing the resilience of structures in seismic-prone areas.

This study aims to assess the necessity of updating Albania's seismic code, KTP.N2-89, by benchmarking it against the advanced provisions of Eurocode 8, with a focus on soil classification, seismic design parameters, and performance-based approaches. The research intends to identify deficiencies in the existing code and recommend improvements to strengthen seismic resilience through the integration of modern, comprehensive standards.

2. Comparison of Design Spectra

The design spectrum is a critical parameter in seismic codes. Seismic design primarily relies on representing earthquake-induced forces as an equivalent static force acting on building structures. These forces are determined based on the maximum acceleration response of the structure, which is depicted by either the acceleration or displacement response spectrum. The shape and amplitude of these spectra are influenced by factors such as soil conditions, epicentral distance, earthquake magnitude, duration, and source characteristics. The goal of incorporating earthquake forces in seismic codes like EC8 is to avoid the need for conducting site-specific seismic hazard analyses for various engineering projects in earthquake-prone regions [11]. While the effects of some parameters can be studied independently, the interaction of multiple factors must be considered together, as they are interrelated. The damping ratio and structural vibration period are additional parameters that affect the response spectra.

Both Eurocode 8 (EC8) and KTP.N2-89 provide zonation maps and response spectra as essential components for seismic design, helping to determine how buildings should respond to seismic forces. Eurocode 8 (EC8) incorporates two distinct types of spectra: Type 1, which is applied to far-field seismic events, and Type 2, which is used for near-field events. The choice between these two types of spectra depends on the characteristics of the earthquakes that contribute most to the seismic hazard at a given site, as determined through probabilistic hazard assessment. Specifically, if the dominant earthquakes in the region have a surface-wave magnitude (M_s) of 5.5 or less, Eurocode 8 recommends using the Type 2 spectrum. However, if the surface-wave magnitude exceeds 5.5, the Type 1 spectrum should be used. This differentiation accounts for the impact of earthquake proximity and magnitude on the seismic forces experienced by buildings. In contrast, KTP-89, the Albanian seismic design code, adopts a more simplified approach by defining only one type of spectrum. This spectrum is determined based on the seismic zone of the site, as well as other relevant factors such as local geological conditions and the expected seismic activity. Unlike Eurocode 8, which differentiates between near-field and far-field effects, KTP.N2-89 uses a single spectrum to cover a broader range of seismic scenarios, making it more generalized in its approach to seismic design.

The ordinates of the elastic design spectra for both Eurocode 8 (EC8) and KTP.N2-89 are presented through their respective expressions in Table 2. In this table, β represents the lower bound factor for the horizontal design spectrum, with the recommended value of β being 0.2. In EC8, seismic hazard is quantified by a parameter known as the reference peak ground acceleration at the rock surface for a reference return period. For the non-collapse performance level, EC8 recommends a reference return period of 475 years, which corresponds to a 10% probability of exceedance within 50 years.

In Eurocode 8, the design ground acceleration (a_g) is determined by multiplying the reference peak ground acceleration by the importance factor (γI). On the other hand, the Albanian seismic code (KTP.N2-89) divides the territory into seismic zones based on increasing seismicity, following the seismic intensity scale (MSK-64). For the purposes of seismic design, only the zones with seismic intensities between VII and IX are considered. These are classified as follows: Intensity VII zone (low seismicity), Intensity VIII zone (moderate seismicity), and Intensity IX zone (high seismicity). KTP-89 assigns a coefficient of zone acceleration that ranges from 0.08 to 0.42, depending on the seismic zone and the soil category.

In Table 2, S denotes the soil factor defined in Eurocode 8, which is determined based on the type of ground at the site. This factor accounts for the influence of soil conditions on seismic responses. Additionally, η represents the damping correction factor, with a reference value of $\eta = 1$ applied for a typical 5% viscous damping, which is the standard assumption for most building designs.

The elastic design spectra are illustrated in Fig. 1, where the expressions from Table 2 are used to plot the spectra for the different soil types specified in both Eurocode 8 and KTP-89. These spectra reflect the seismic response for various soil conditions, enabling more accurate seismic design based on the site's specific characteristics. Since the case study building is located in a zone characterized by moderate seismicity, as indicated by the Albanian seismic zonation map, the response spectra for the Albanian seismic code (KTP.N2-89) are provided specifically for the moderate seismicity zone. This allows for a focused comparison of the seismic effects under the typical conditions of this region.

Table 2. Ordinates of spectra for EC8 and KTP.N2-89

Eurocode 8	**KTP.N2-89**
$0 \le T \le T_B$ $Se = a_g \cdot S\left[1 + \frac{T}{T_B}(2.5 \cdot \eta - 1)\right]$ $T_B \le T \le T_C$ $Se = a_g \cdot S \cdot 2.5 \cdot \eta$ $T_C \le T \le T_D$ $Se = a_g \cdot 2.5 \cdot \eta \cdot S\left[\frac{T_C}{T}\right]$ $T_D \le T \le 4s$ $Se = a_g \cdot 2.5 \cdot \eta \cdot S\left[\frac{T_C T_D}{T^2}\right]$	$S_a = k_E \cdot k_r \cdot \psi \cdot \beta \cdot g$ k_r – building importance coefficient (Table 5 of KTP) ψ – structural coefficient (Table 4 of KTP-89) g – gravitational constant **- Soil category I** $0.65 \le \beta_i = \frac{0.7}{T_i} \le 2.3$ **- Soil category II** $0.65 \le \beta_i = \frac{0.8}{T_i} \le 2.0$
Corner Periods of design spectra defined in EC8	**- Soil category III**

Soil type A
Type 1: $T_B = 0.15,\ T_C = 0.4,\ T_D = 2$
Type 2: $T_B = 0.05,\ T_C = 0.25,\ T_D = 1.2$

Soil type B
Type 1: $T_B = 0.15,\ T_C = 0.5,\ T_D = 2$
Type 2: $T_B = 0.05,\ T_C = 0.25,\ T_D = 1.2$

Soil type C
Type 1: $T_B = 0.2,\ T_C = 0.6,\ T_D = 2$
Type 2: $T_B = 0.1,\ T_C = 0.25,\ T_D = 1.2$

Soil type D
Type 1: $T_B = 0.2,\ T_C = 0.8,\ T_D = 2$
Type 2: $T_B = 0.1,\ T_C = 0.3,\ T_D = 1.2$

Soil type E
Type 1: $T_B = 0.15,\ T_C = 0.5,\ T_D = 2$
Type 2: $T_B = 0.05,\ T_C = 0.25,\ T_D = 1.2$

$$0.65 \le \beta_i = \frac{1.1}{T_i} \le 1.7$$

k_E table	Seismic Intensity (MSK-64)		
Soil type	VII	VIII	IX
I	0.08	0.16	0.27
II	0.11	0.22	0.36
III	0.14	0.26	0.42

Figure. 1 presents the design spectra proposed by both Eurocode 8 (EC8) and KTP.N2-89. As noted earlier, there are several differences between the two codes, both in terms of the spectral form and the spectral amplitude. KTP.N2-89 does not account for the soil factor, using the same spectral amplitude peak values for all three soil types. In contrast, EC8 provides different spectral amplitudes, incorporating the soil factor and distinguishing between near-field and far-field seismic conditions. This results in a more detailed and site-specific approach in EC8 compared to the more generalized approach in KTP.N2-89.

The comparison between the seismic design spectra proposed by Eurocode 8 (EC8) and KTP.N2-89 reveals significant differences in their methodologies and applications, particularly regarding the incorporation of soil factors and the treatment of seismic conditions. Eurocode 8 adopts a more nuanced approach by differentiating spectral amplitudes based on soil type and seismic conditions, which enhances the site-specific applicability of the design spectra. In contrast, KTP.N2-89 employs a more generalized framework that does not account for variations in soil characteristics, leading to uniform spectral amplitude peak values across different soil types. This fundamental difference underscores the importance of site-specific seismic design, as highlighted by various studies that emphasize the role of soil conditions in seismic response [12-13].

The incorporation of soil factors in EC8 allows for a more refined assessment of seismic hazards, which is critical for ensuring the structural integrity of buildings in varying geological contexts. Research indicates that the classification of soil types and their corresponding effects on seismic response are essential for accurate design and risk assessment [12-13]. For instance, the Eurocode categorizes soil into different classes, which directly influences the design spectra and the expected seismic demands on structures. This classification system is supported by empirical data and site characterization studies that demonstrate the variability of seismic responses based on soil conditions. In contrast, the KTP.N2-89 standard's uniform approach may lead to inadequate designs in regions with diverse geological profiles, as it fails to account for the unique seismic characteristics associated with different soil types.

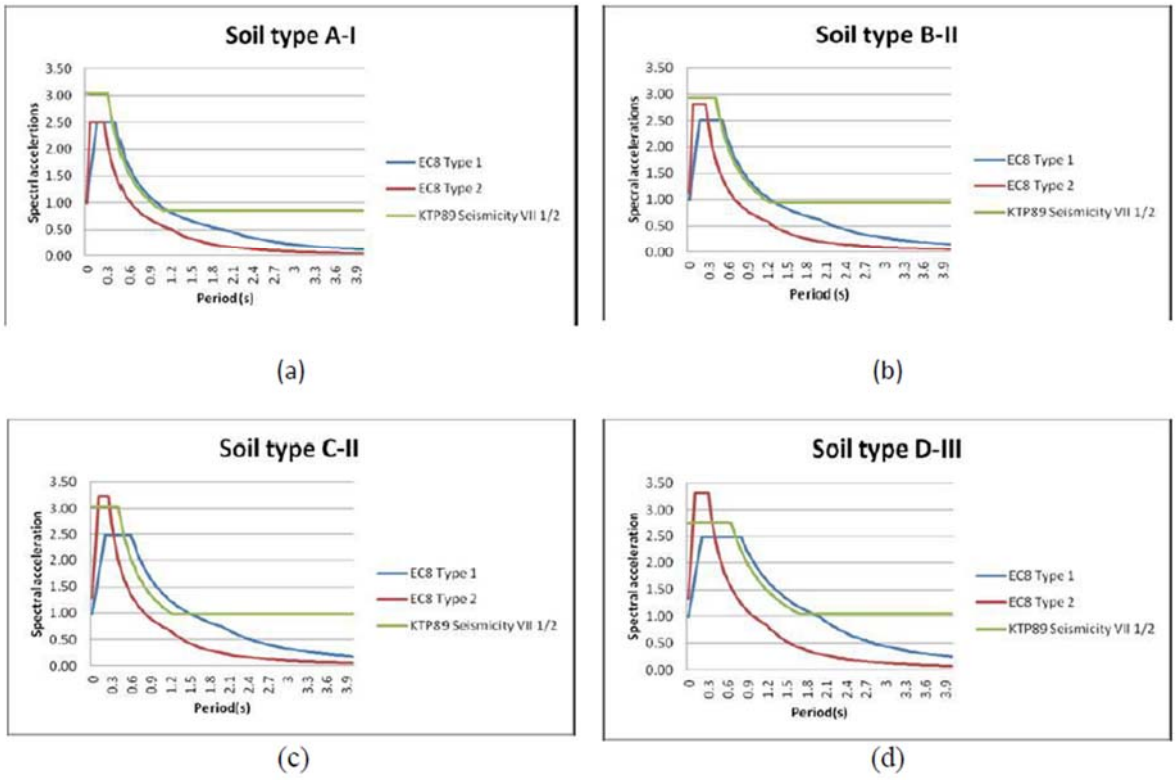

Fig. 1 Elastic design spectra defined in EC 8 and KTP.N2-89

Furthermore, the distinction between near-field and far-field seismic conditions in EC8 provides an additional layer of specificity that is absent in KTP.N2-89. Near-field earthquakes, which occur close to the fault line, often produce different ground motion characteristics compared to far-field events. Eurocode 8's consideration of these differences allows for more accurate predictions of structural behavior under varying seismic scenarios [13]. This is particularly relevant in regions prone to significant seismic activity, where the implications of ground motion characteristics can drastically affect the performance of structures during an earthquake. The ability to tailor design spectra to specific seismic conditions enhances the resilience of structures, as evidenced by studies that have analyzed the performance of buildings designed under EC8 compared to those designed under more generalized codes [13].

The differences between Eurocode 8 and KTP.N2-89 highlight the critical importance of site-specific considerations in seismic design. Eurocode 8's incorporation of soil factors, differentiation between near-field and far-field conditions, and reliance on empirical data collectively contribute to a more comprehensive and effective approach to seismic design. In contrast, the generalized framework of KTP.N2-89 may lead to inadequate designs in diverse geological contexts, emphasizing the need for codes that are adaptable to local conditions and informed by rigorous scientific research [12-14].

3. Description of The Case Study Building for Comparative Assessment

The building considered in this study is an 8-story frame-shear wall structure. It has a total height of 25.2 meters, with each story having an elevation of 3.15 meters. The building's floor plan dimensions are 13.85 meters by 27.85 meters, providing a rectangular layout. This structural configuration includes both reinforced concrete frames and shear walls, which contribute to its overall seismic resistance by enhancing stiffness and reducing lateral movement under earthquake loading. The analysis of this building aims to assess its seismic performance by simulating its behavior under dynamic analyses.

To evaluate the seismic response of the building, elastic analyses were performed using the response spectrum method with the ETABS software [15]. The seismic analysis was carried out separately for both the longitudinal and transverse directions to capture the structural response under different loading scenarios. A sample of the finite element model used in the analysis is shown in Fig. 2. This model accurately represents the building's geometry, material properties, and boundary conditions, providing a reliable tool for evaluating its seismic behavior under various ground motion inputs.

The beams and columns of the building were modeled using frame elements, while the walls were represented using shell elements to accurately simulate their behavior under seismic loading. The slabs were considered as rigid diaphragms at each story level, effectively distributing lateral forces across the structure. The unit weight of concrete was taken as 25 kN/m^2, and the Young's modulus was assumed to be 28,000 MPa, typical for reinforced concrete. A damping ratio of 5% was applied in all modes of vibration to reflect the typical behavior of reinforced concrete structures.

The building is located in a moderate seismicity zone, as indicated by the seismicity map of the KTP-89 code and the building's technical report. For the seismic analysis, the reference peak ground acceleration was taken to be 0.25g, as recommended in the KTP.N2-89 code [16]. This same value was also used for the EC8 analysis to facilitate a direct comparison between the two codes' seismic design approaches.

4. Earthquake Analyses

The building's seismic response was analyzed considering 12 modes of vibration. The modes, along with their corresponding periods and participating mass ratios, are presented in Table 3. The first and third modes involve lateral vibrations in the y and x directions, respectively, while the second mode is a torsional mode. These modes are critical in understanding how the building responds to seismic forces, as they represent the primary directions of deformation and the distribution of mass during an earthquake. The participation of these modes in the total building response is quantified through the participating mass ratios, which are also included in the table for reference.

As shown in Table 3, the cumulative sum of the participating mass ratios exceeds 90% for the first seven modes in the y direction and for the first ten modes in the x direction. This indicates that the majority of the building's seismic response in both directions is captured by these modes, highlighting their significance in the overall dynamic behavior of the structure during an earthquake. The remaining modes contribute less significantly to the response, and thus can be considered as having a minimal impact on the seismic performance of the building.

The base shears of the case were determined from seismic analysis using the design spectra corresponding to 5% critical damping and assuming a fixed-base condition. Seismic analyses were conducted for each type of soil defined in KTP.N2-89, as well as their equivalents in EC8. The results are presented in Fig. 3, where the horizontal axis represents the different soil types as classified in both codes. As shown in Table 1, there are differences in soil classification between the two codes. In the KTP-89 classification, Soil Type II is considered equivalent to Soil Types B and C in EC8, Soil Type I corresponds to Soil Type A, and Soil Type III aligns with Soil Type D in EC8.

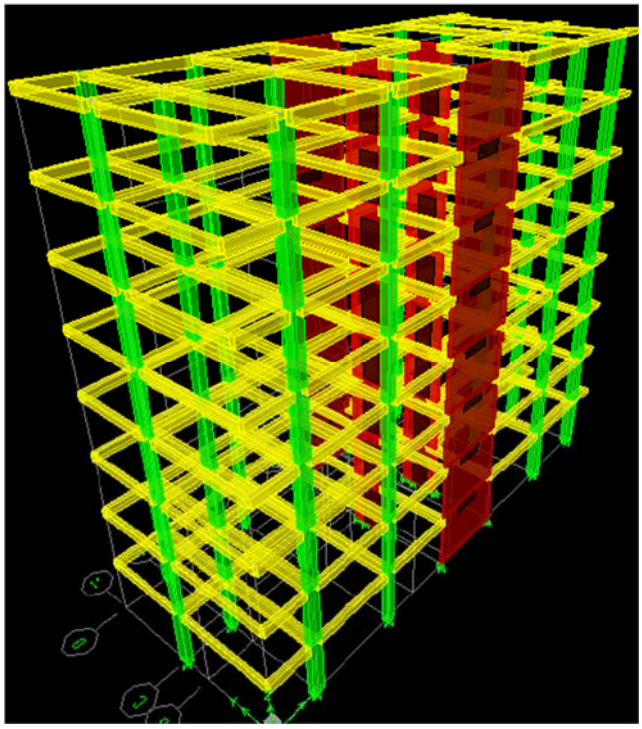

Fig. 2. 3D View of the 3D model of the building

Table 3 First 12 modes and modal particiapating ratios of the building

		Individual mode (%)		Cumulative sum (%)	
Mode	Period	Ux	Uy	Ux	Uy
1	0.984	0.03	72.31	0.03	72.31
2	0.876	1.08	0.68	1.11	72.99
3	0.634	68.02	0.01	69.13	73.00
4	0.264	0.01	13.33	69.13	86.32
5	0.221	0.10	0.35	69.24	86.67
6	0.144	17.71	0.00	86.94	86.67
7	0.117	0.00	5.66	86.95	92.33
8	0.097	0.02	0.26	86.96	92.59
9	0.065	0.00	2.88	86.96	95.47
10	0.060	6.77	0.00	93.73	95.48
11	0.056	0.01	0.35	93.74	95.83
12	0.042	0.00	1.27	93.74	97.09

As illustrated in Fig. 3, the base shears become more significant for soft soils due to the lower fundamental frequency of the building. This is particularly noticeable for structures that experience more pronounced seismic response on softer ground. The results also reveal that EC8 Type 1 produces the highest base shears across all soil types. This is because the spectral ordinate corresponding to the building's fundamental period, which is 0.98 seconds, plays a crucial role in EC8 Type 1, as it captures the response of the building at its fundamental vibration period. On the other hand, EC8 Type 2 yields base shear values that are closer to those of KTP-89, but this alignment occurs primarily for very soft soils (Soil Type D-III). The reason for this is the higher soil factor defined in EC8 for Soil Type D-

III, which is set at 1.8, reflecting the amplified seismic response expected for such soil conditions. These findings highlight the importance of using the far-field earthquake spectrum (Type 1) for flexible structures, especially when soft soils are present, as this approach accounts for the more significant seismic forces that such structures may experience, leading to more conservative and potentially safer design outcomes.

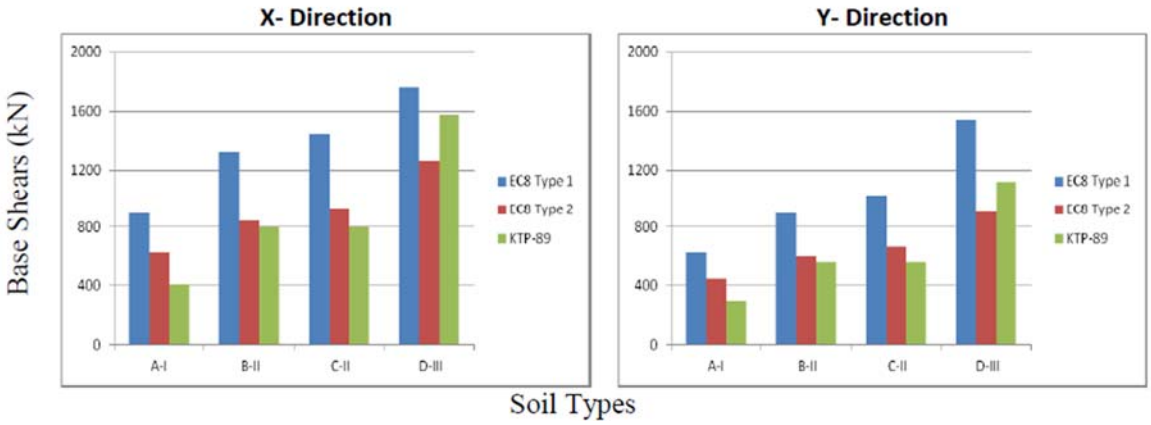

Fig. 3. Variation of base shear forces of the building considering different types of soil

5. Conclusions

This study evaluates the seismic analysis of a representative case study building, which is commonly found in the reinforced concrete (RC) building stock in Albania. The primary focus of the analysis is on the design spectrum, which plays a crucial role in determining the seismic forces acting on the structure. A detailed comparison is made between the design spectra defined in Eurocode 8 (EC8) and the Albanian seismic code KTP.N2-89, with a particular emphasis on identifying and discussing the key differences between the two. One of the significant differences is that EC8 takes into account two important parameters that are not considered in KTP.N2-89: the site effect and the distinction between near-field and far-field seismic events. EC8 introduces a site factor (S) to account for varying soil conditions, which can significantly affect the building's seismic response. Additionally, EC8 differentiates between near-field and far-field earthquake effects, providing a more nuanced approach to seismic design based on the proximity of the earthquake's epicenter. These factors are not addressed by KTP.N2-89, making EC8 more comprehensive in terms of considering the influence of both soil conditions and earthquake source characteristics. The study discusses these differences in detail, offering insights into how they impact the overall seismic design and performance of buildings in earthquake-prone regions.

Base shear demands tend to increase as the soil becomes softer, with the highest base shear values observed for Soil Type D-III (very soft soil). Eurocode 8 (EC8) Type 1 consistently produces the maximum base shear values across all soil types, reflecting the more conservative approach for seismic design. In contrast, KTP-89 generally results in lower base shear values compared to EC8 Type 2, except for Soil Type D-III. This discrepancy is due to the significant role of the k_E factor, which is particularly important for very soft soils. The k_E factor, defined in KTP.N2-89, accounts for the amplification of seismic forces in such soil conditions, leading to higher base shear values in KTP.N2-89 for Soil Type D-III compared to EC8 Type 2.

References

[1] KTP-N.2-89 (1989) Technical aseismic regulations. Publication of Academy of Sciences and Ministry of Constructions (in Albanian). Tirana, Albania.
[2] Abrahamczyk, L., Penava, D., Haweyou, M., Anić, F., Schultz, A. E., & Rautenberg, J. (2021). Assessment of damage to modern reinforced concrete buildings – engineering analysis of the m6.4 albania earthquake, 26th of nov. 2019. Proceedings of the 8th International Conference on Computational Methods in Structural Dynamics and Earthquake Engineering (COM. https://doi.org/10.7712/120121.8531.19114.
[3] Bilgin, H. Seismic assessment of residential building typologies: emphasis on masonry buildings. Bull Earthquake Eng (2024). https://doi.org/10.1007/s10518-024-02004-w.
[4] Leti, M. and Bilgin, H. (2024). Investigation of seismic performance of a premodern RC building typology after the November 26, 2019 earthquake. Structural Engineering and Mechanics, 89(5), 491–505. https://doi.org/ 12989/sem.2024.89.5.491.
[5] Bilgin H, Fule Z, Ozmen HB. Numerical study to evaluate the structural response of the basilica of St. Sotiri. Res. Eng. Struct. Mater., 2023; 9(2): 309-329.
[6] Lu, B. Y. and Wang, G. (2011). A comparative study of seismic performance defined by Chinese code and eurocode8 on seismic design of bridges. Applied Mechanics and Materials, 90-93, 3108-3116. https://doi.org/10.4028/www.scientific.net/amm.90-93.3108.
[7] Rozman, M. and Fajfar, P. (2009). Seismic response of a rc frame building designed according to old and modern practices. Bulletin of Earthquake Engineering, 7(3), 779-799. https://doi.org/10.1007/s10518-009-9119-4.
[8] Aliaj, S., Adams, J., Halchuk, S., Sulstarova, E., Peçi, V., & Muço, B. (2004). Probabilistic seismic hazard maps for albania.. https://doi.org/10.4095/226354.
[9] EN 1998-1. European seismic design code. (2004). “Design of structures for earthquake resistance. Part 1: General rules, seismic actions and rules for buildings”.
[10] Bosco, M., Ghersi, A., & Marino, E. M. (2009). On the evaluation of seismic response of structures by nonlinear static methods. Earthquake Engineering &Amp; Structural Dynamics, 38(13), 1465-1482. https://doi.org/10.1002/eqe.911.
[11] Elghazouli, Ahmed Y., (2009). Seismic design of buildings to Eurocode 8, Spon Press.
[12] Sertçelik, F., Livaoğlu, H., Sertçelik, İ., & Iblikçi, S. (2018). Investigation of site characterization in akdeniz region by using seismic refraction and surface wave methods. International Journal of Applied and Physical Sciences, 4(3). https://doi.org/10.20469/ijaps.4.50003-3.
[13] Khose, V. N., Singh, Y., & Lang, D. H. (2012). A comparative study of design base shear for rc buildings in selected seismic design codes. Earthquake Spectra, 28(3), 1047-1070. https://doi.org/10.1193/1.4000057.
[14] Bulajić, B. Đ., Manić, M., & Ladjinovic, D. (2012). Towards preparation of design spectra for serbian national annex to eurocode 8: part ii. usage of the uhs approach instead of normalized spectral shapes scaled by a single psha parameter. Facta Universitatis - Series: Architecture and Civil Engineering, 10(3), 259-274. https://doi.org/10.2298/fuace1203259b.
[15] ETABS Software, (2010). Extended 3-D Analysis and Design of Structural Systems: Computers and Structures. Inc. Berkeley, California.
[16] Aliaj, S., Kociu, S., Muco, B. and Sulstarova, E. (2010). Seismicity, seismotectonics and seismic hazard assessment in Albania.

MIM Research Group Research & Design
www.jrede.org

Research Article

Evaluating spatial resolution enhancement on impervious surface detection using support vector machine

Mustafa Hayri Kesikoglu*[1,2a]

[1]*Department of Civil Engineering, Faculty of Engineering and Natural Sciences, Uşak University, 64000, Uşak, Türkiye*
Department of Urban and Regional Planning, Faculty of Architecture and Design, Uşak University, 64000, Uşak, Türkiye

Article Info

Article History:
Received: 11 Nov 2024
Accepted: 4 Dec 2024

Keywords:
Classification;
Impervious surface areas (ISA);
Landsat 8;
Pan-sharpening;
Remote sensing;
Support Vector Machine (SVM)

Abstract

Impervious surface areas (ISA) have caused significant environmental and hydrological changes as a result of increasing population and urban expansion. This study investigated the effects of high spatial resolution images obtained using Gram-Schmidt pan-sharpening method and multispectral Landsat 8 Operational Land Imager (OLI) satellite imagery on classification accuracy for ISA detection. Support vector machine (SVM) was used to classify ISA and other surfaces in Uşak province. The classification results indicated that the overall accuracy of the pan-sharpened image was 92.5% and kappa value was 85%. Compared to the multispectral image, these values represent increases of 2.5% and 5%, respectively. The findings show that pan-sharpened satellite images are a valuable tool for ISA detection. This method can be particularly effective for environmental management and sustainable urban planning and design in urban areas. Additionally, the results of this study can be generalized to other regions with similar geographical and urban characteristics. This approach provides a foundation for more accurate mapping of ISA and more effective management of urban environments.

1. Introduction

Impervious surface areas (ISA), which prevent water infiltration into the soil, encompass roads, pavements, parking lots, building roofs, and concrete surfaces. Due to increasing population and related demands, impervious surfaces have expanded rapidly in areas designated for residential, commercial, and transportation purposes [1]. The detection of ISA is crucial for designing both natural environments and urban development. In this context, remote sensing technologies can analyze extensive areas rapidly and reliably. Remote sensing for ISA detection provides quicker results compared to fieldwork and other manual methods, and multispectral satellite imagery also enables detailed spectral analysis [2-4].

ISA significantly impact the hydrological cycle by preventing surface water infiltration into the soil. Factors such as urbanization and population growth contribute to the widespread increase of ISA. For instance, Omurakunova et al. (2020) highlighted that urban sprawl in Kyrgyzstan has led to a significant expansion of impervious surfaces, which correlates with economic development and urban designing strategies [5]. The increase in ISA results in heightened surface runoff, which can lead to increased flood risks, particularly in densely

*Corresponding author: hayri.kesikoglu@usak.edu.tr
[a]orcid.org/0000-0001-5199-0815;
DOI: http://dx.doi.org/10.17515/rede2024.003bu1111rs

populated urban areas. Dong et al. (2021) emphasized that the rapid urbanization of cities like Beijing has resulted in a marked increase in impervious surfaces, which are defined as materials that prevent water infiltration, such as roads and rooftops [6].

The environmental impacts of ISA are multifaceted, manifesting in various issues such as elevated surface temperatures and alterations in local microclimates. Tian et al. (2018) noted that the transformation of natural landscapes into anthropogenic ones due to ISA expansion significantly exacerbates the urban heat island effect, which is a critical concern for urban environmental quality [7]. Furthermore, Liang et al. (2022) discussed how intensive economic activities and rural-to-urban migration contribute to the growth of built-up areas and ISA, leading to ecological challenges [8]. The consequences of increased impervious surfaces extend beyond immediate hydrological impacts; they also affect urban climate dynamics and water quality, as highlighted by Long et al. (2020), who noted that the expansion of ISA often comes at the decrease of vegetation cover, further intensifying urban heat effects [9].

Monitoring and accurately mapping ISA are essential for effective environmental management, water resource preservation, and urban design. The use of remote sensing technologies has become increasingly prevalent in this regard. For example, Qiao et al. (2018) examined the distribution of ISA in different functional zones of Beijing, emphasizing the importance of remote sensing in understanding urban environmental changes [10]. Similarly, Hidayati & Suharyadi (2019) conducted a comparative study of different indexes to detect ISA using Landsat 8 OLI data, underscoring the complexity of accurately mapping these surfaces [11].

Image resolution is one of the most effective factors in correctly classifying ISA. Panchromatic sharpening (pan-sharpening) integrates high spatial resolution from panchromatic images with the spectral information from lower resolution multispectral images, resulting in enhanced image quality that is crucial for accurate classification tasks. The pan-sharpened high-resolution satellite images significantly affect the accuracy of land cover classification studies using various machine learning algorithms. For instance, Liu et al. (2023) suggested a pan-sharpening model based on feature fusion and attention modules, demonstrating that their method improved classification accuracy when applied to remote sensing images [12]. This aligns with findings from Li and Cheng (2019) [13], who utilized a Convolutional Neural Network (CNN)-based pan-sharpening method for Landsat 8 images, achieving notable enhancements in classification performance due to the improved spatial resolution of the resulting images. Ghayour et al. (2021) compared various machine learning methods using Landsat 8 OLI and Sentinel-2 satellite images for land cover classification, revealing that Support Vector Machine (SVM) outperformed other methods when high-resolution images were employed. This suggests that the integration of pan-sharpening techniques can significantly enhance the effectiveness of SVM in land cover classification tasks [14]. Similarly, Khateri et al. (2020) introduced a variational approach for fusing multispectral images and panchromatic, emphasizing the importance of spatial and spectral consistency in improving classification accuracy [15]. Their findings indicate that the use of high-resolution panchromatic images can lead to better delineation of land cover types, which is critical for environmental monitoring and urban planning.

This study aims to assess the effect of multispectral satellite imagery and pan-sharpened higher spatial resolution multispectral imagery on the classification accuracy of ISA. The study has shown that using pan-sharpened satellite images to determine impervious surfaces in urban areas provides higher accuracy results than multispectral images. The results obtained with the SVM algorithm, one of the machine learning methods, emphasize that pan-sharpened images are an important tool for urban area analysis. Although the

study is an evaluation conducted in Uşak province, it can provide generalizable results for other regions with similar geographical and urban characteristics. The obtained findings constitute an important step for more accurate and detailed analyses in urban planning and design, environmental management, and sustainability.

2. Materials

2.1. Study area and data

Uşak province is situated in the Inner Aegean Section, connecting Central and Western Anatolia within the Aegean region of Türkiye. The province covers an area of approximately 5341 square kilometers and has a diverse topography characterized by hills and valleys, which influence its urban development patterns [16]. Uşak has rapidly received migration and grown with the country's urbanization movement. Due to the increasing population and urbanization, it is led to significant transformations in land use and land cover. This situation has resulted in an increase in ISA. ISA detection is of great importance in the natural environment management, monitoring and designing rural-urban areas .

For this study, Landsat 8 Operational Land Imager (OLI) data from September 23, 2018, with a spatial resolution of 30 meters, was utilized to assess ISA in Uşak Province. The Landsat 8 satellite provides medium-resolution imagery that is essential for accurately mapping land use land cover detections, including the extent of impervious surfaces. The data allows for the application of various remote sensing techniques and machine learning algorithms to classify land cover types effectively. Previous studies have demonstrated the efficacy of Landsat data in monitoring land use land cover detections, particularly in rapidly urbanizing areas. The general characteristics of the Landsat 8 satellite data and satellite image used in the study are shown in Fig. 1 and Fig. 2. In this study, the classification process was performed by selecting 3000 pixels for the training area and 1000 pixels for the validation process. The same training and test data were used for both MS and pan-sharpened images.

Landsat 8	Bands	Wavelength (micrometers)	Resolution (meters)
Operational Land Imager (OLI) and Thermal Infrared Sensor (TIRS)	Band 1 - Ultra Blue (coastal/aerosol)	0.43 - 0.45	30
	Band 2 - Blue	0.45 - 0.51	30
	Band 3 - Green	0.53 - 0.59	30
	Band 4 - Red	0.64 - 0.67	30
	Band 5 - Near Infrared (NIR)	0.85 - 0.88	30
	Band 6 - Shortwave Infrared (SWIR) 1	1.57 - 1.65	30
	Band 7 - Shortwave Infrared (SWIR) 2	2.11 - 2.29	30
	Band 8 - Panchromatic	0.50 - 0.68	15
	Band 9 - Cirrus	1.36 - 1.38	30
	Band 10 - Thermal Infrared (TIRS) 1	10.60 - 11.19	100 * (30)
	Band 11 - Thermal Infrared (TIRS) 2	11.50 - 12.51	100 * (30)

Fig. 1. Landsat 8 satellite data features [3]

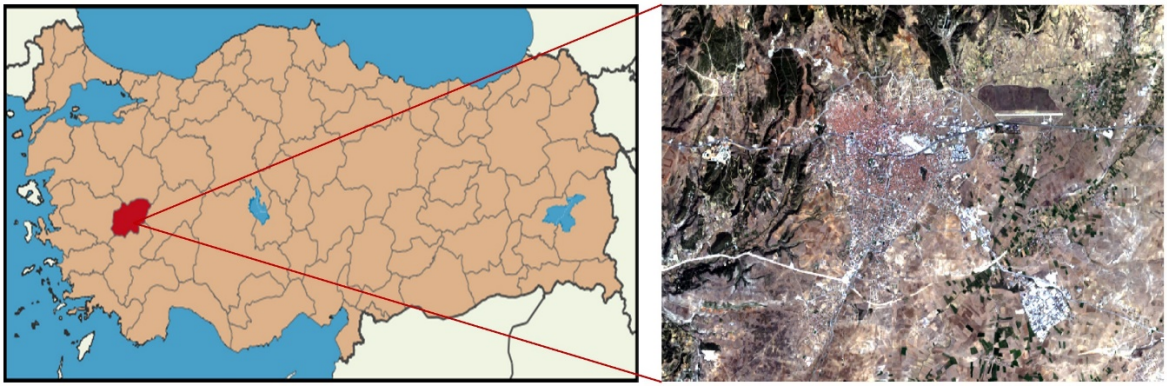

Fig. 2. Study area

3. Methodology

ISA, one of the areas that directly affect urban area design, were determined using the pixel-based SVM method. The data sets and process steps used to determine these areas are shown in Fig. 3.

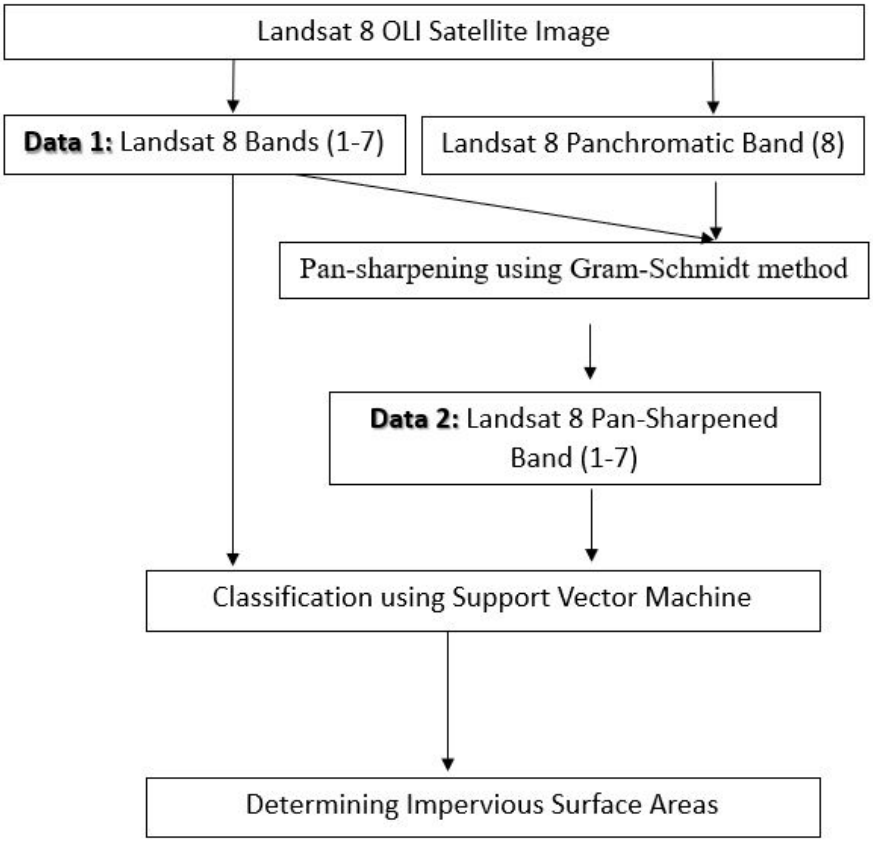

Fig. 3. General framework of the experimental study

The study created the multispectral data 1 (Band 1-7) by combining the ultra-blue, visible (Blue, Green, Red), near-infrared, and short-wave infrared bands of the Landsat 8 OLI satellite image. In the second step, pan-sharpened multispectral data 2 was obtained using the Gram-Schmidt method. Pan-sharpening integrates the high spatial resolution of the panchromatic band with the spectral resolution of the multi-spectral (MS) bands. As a result, the data 2 referred to as pan-sharpened becomes a multi-spectral image with enhanced spatial resolution. While the original data has a spatial resolution of 30 meters,

the pan-sharpened data achieves a spatial resolution of 15 meters. In the third step, each data set was classified into two classes IS and other fields. The SVM, one of the machine learning methods, was used to classify the data 1 and 2 images. In the fourth step Classification results were evaluated using overall accuracy and kappa statistic metrics.

3.1. Gram-Schmidt pan-sharpening method

The Gram-Schmidt pan-sharpening method is a widely recognized technique to enhance the spatial resolution of multispectral images by integrating high-resolution panchromatic data. This method, introduced by Laben and Brower in 2000 [17], utilizes the Gram-Schmidt process to achieve a more accurate fusion of spectral and spatial information, resulting in images that maintain the spectral integrity of the original multispectral data while enhancing spatial details. The method operates by transforming the multispectral bands into a new space where the panchromatic image can be incorporated effectively, thereby minimizing color distortion and maximizing image sharpness [18].

The Gram-Schmidt pan-sharpening method offers several advantages that make it a preferred choice to enhance the spatial resolution of multispectral images. One of the primary benefits of this method is its ability to maintain the spectral integrity of the original multispectral data while improving spatial resolution. This is achieved through a mathematical transformation that minimizes color distortion, resulting in images that are both sharp and true to their original colors [18]. Additionally, the Gram-Schmidt method is known for its robustness in handling various types of remote sensing data, making it versatile across different applications. For instance, it has been successfully applied to high-resolution satellite imagery, such as WorldView-2, where it demonstrated superior performance compared to other pan-sharpening techniques like Intensity-Hue-Saturation (IHS) and Principal Component Analysis (PCA) [19, 20]. The method's effectiveness in reducing spectral distortion while enhancing spatial details has been highlighted in multiple studies, indicating its reliability in producing high-quality fused images suitable for various remote sensing studies, including vegetation and land use/land cover classification mapping [21, 22]. Moreover, the Gram-Schmidt method is computationally efficient, allowing for faster processing times without compromising the quality of the output images. This efficiency is particularly beneficial when working with large datasets, as it enables researchers to obtain high-resolution images quickly, facilitating timely analysis and decision-making [18].

3.2. Support vector machine

SVM is a powerful supervised machine learning method primarily utilized for classification studies, although it can also be applied to regression problems. SVM works by finding the optimal hyperplane that separates data points of different classes in a high-dimensional space. The key idea is to maximize the margin between the closest points of each class, known as support vectors. This approach allows SVM to create a robust decision boundary that generalizes well to unseen data, making it particularly effective in scenarios with high-dimensional feature spaces [23].

One of the significant advantages of SVM is its ability to handle linear and non-linear classification problems using kernel functions. These kernels transform the input data into a higher-dimensional space where a linear separation is possible, even if the original data is not linearly separable. Common kernel functions include sigmoid, radial basis function (RBF), and polynomial kernels, which provide flexibility in modeling complex relationships within the data [23, 24]. Additionally, SVM is known for its robustness against overfitting, especially in high-dimensional spaces, due to its structural risk minimization principle, which balances model complexity and training error [25]. Its ability to work well with small

to medium-sized datasets while maintaining high accuracy makes it a popular choice among researchers and practitioners. Furthermore, SVM's performance can be enhanced through techniques such as parameter tuning and the use of ensemble methods, further solidifying its position as a leading algorithm in the machine-learning community [26]. In the study, RBF kernel was used and kernel scale was 1.

4. Results and Discussion

In this study, a high spatial resolution sharpened MS color image was created by combining the spectral resolution of multispectral (MS) bands (Band 1-7) with the high spatial resolution of the panchromatic band (Band 8) of Landsat 8 OLI satellite imagery by pan-sharpening process. The pan-sharpening process was performed using the Gram-Schmidt method. One of the advantages of this method is that multi-band data can be processed at once. MS image in RGB band combination (Fig. 4a), panchromatic band image (Fig. 4b), and pan-sharpened image (Fig. 4c) are seen in Fig. 4.

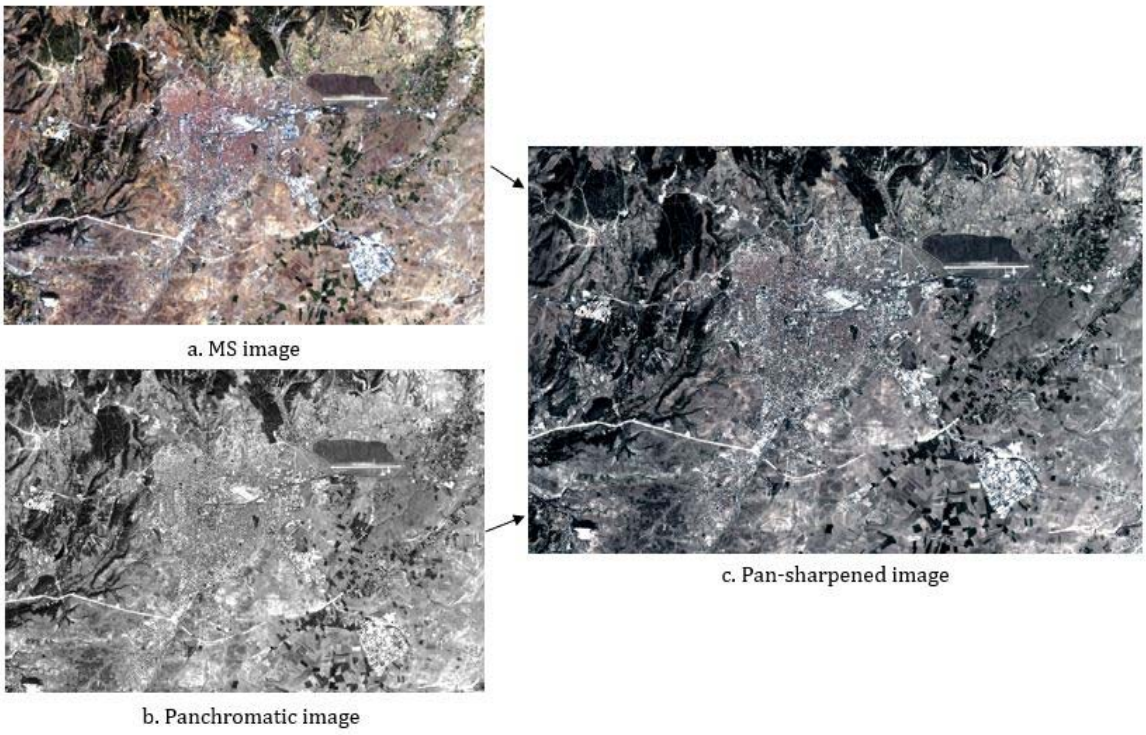

Fig. 4 a. MS image, b. Panchromatic image, c. Pan-sharpened image

The classification process was performed based on the pixel-based supervised classification approach. ISA and other areas were distinguished using the SVM method, which is one of the machine learning methods. The MS and pan-sharpened classification images are shown in Fig. 5. The classification process was analyzed using the general accuracy and kappa quantitative evaluation metrics. The obtained quantitative evaluation results are shown in Table 1.

Table 1. Classification accuracies

Dataset	Overall Accuracy	Kappa
MS image	90%	80%
Pan-sharpened image	92.5%	85%

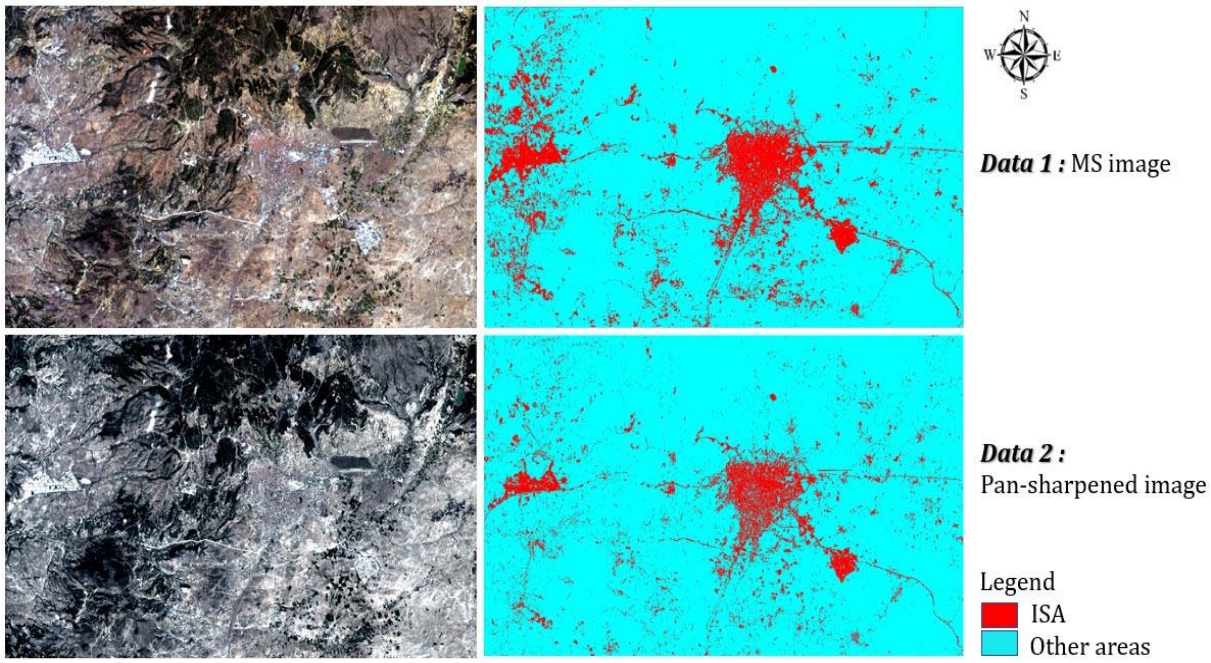

Fig. 5. Classified MS and pan-sharpened images

When the classification images (Fig. 5) are examined, it is seen that the ISA and other areas obtained with the pan-sharpened classification image (Data 2) are more accurate than those obtained with the MS classification image (Data 1) in urban areas. Hence, pan-sharpened image provided more distinct boundaries for ISA detection. The classification performance improved, particularly in areas of urban density. When the quantitative results (Table 1) are examined, it is determined that the overall accuracy of the pan-sharpened image is 2.5% higher than the classification accuracy of the MS image, and the kappa statistic value is 5% higher. In other words, the overall accuracy and kappa value were calculated as 92.5% and 85%, respectively. These results demonstrate that the pan-sharpening process positively impacts classification accuracy by enhancing spatial resolution. The increase detected in the kappa statistic value indicates a significant improvement in the reliability of the classification. According to the results obtained from the study, it is understood that the ISA located in the center and west of the image can be detected more accurately as the spatial resolution increases.

In this study, it has been shown that the detection of ISA using satellite images with increased spectral resolution by Gram-Schmidt panchromatic sharpening gives successful results. Some studies have supported that this method can significantly improve classification accuracy when applied to various land cover classifications, including wetlands, forests, and urban areas [20, 27]. Furthermore, the Gram-Schmidt method has been compared with other pan-sharpening techniques, such as the Brovey transform and Principal Component Analysis (PCA), revealing its superior performance in terms of spectral fidelity and spatial resolution [20]. Studies have shown that the Gram-Schmidt method can effectively reduce artifacts commonly associated with other pan-sharpening methods, making it a reliable choice for producing high-quality fused images [28]. However, the application of panchromatic sharpening is not without challenges. Park, Kim [29] noted that while high-spatial-resolution multispectral images produced through pan-sharpening techniques can enhance visual interpretation, they may also distort the spectral information of the original images, complicating analyses that depend on accurate spectral characteristics. This distortion can lead to misclassification in certain contexts, particularly when the spectral properties of the land cover classes are closely related. Consequently, it is crucial to carefully select and evaluate the panchromatic sharpening

algorithms used, as different methods can yield varying results in classification accuracy relying on the specific characteristics of the study area [30].

5. Conclusion

Determination of ISA is an important and frequently monitored situation for the protection and management of the natural environment and monitoring of urban development. The expansion of impervious surfaces due to urbanization poses significant challenges for hydrological cycles and urban environmental quality. The integration of advanced monitoring techniques, particularly remote sensing, is crucial for addressing these challenges and informing sustainable urban planning and design practices. The integration of panchromatic sharpening techniques in satellite image classification studies has demonstrated significant potential for enhancing accuracy across various machine learning algorithms.

This study evaluated the effectiveness of remote sensing technologies for detecting ISA in urban settings. In this study, ISA in the city center of Uşak were analyzed using a pixel-based classification approach. Two different data sets were created, multispectral and pan-sharpened. The effect of the data set used on the classification result was investigated. High spatial resolution images obtained utilizing the Gram-Schmidt pan-sharpening method provided significant advantages in improving classification accuracy for ISA detection. The image classification process was performed using the SVM method, one of the most popular machine learning methods. Comparisons between multispectral and pan-sharpened images showed that pan-sharpening yielded a 2.5% higher overall accuracy and a 5% higher kappa value. This method offers a robust tool for ISA detection and environmental management, especially in areas with high urban density. The study provides foundational insights for environmental sustainability, urban planning, and natural resource conservation.

While the benefits of improved spatial resolution are evident, researchers must remain vigilant regarding the potential for spectral distortion and its implications for classification outcomes. Continued exploration of advanced panchromatic sharpening methods may further refine the balance between spatial enhancement and spectral fidelity, ultimately leading to more reliable remote sensing applications. Future research can explore the efficacy of pan-sharpening with alternative satellite datasets and classification methods on a broader scale.

References

[1] Kesikoglu MH, Ozkan C, Kaynak T. The impact of impervious surface, vegetation, and soil areas on land surface temperatures in a semi-arid region using Landsat satellite images enriched with Ndaisi method data. Environmental Monitoring and Assessment. 2021;193(3):143.

[2] Kesikoglu MH, Cicekli SY, Kaynak T, Ozkan C, editors. The determination of coastline changes using artificial neural networks in Yamula Dam Lake, Turkey. 2017 8th International Conference on Information Technology (ICIT); 2017 17-18 May 2017.

[3] Kesikoğlu MH, Cicekli SY, Kaynak T. The identification of seasonal coastline changes from Landsat 8 satellite data using artificial neural networks and k-nearest neighbor. Turkish Journal of Engineering. 2020;4(1):47-56.

[4] Kesikoglu MH, Atasever UH, Özkan C. The Usage of Rusboost Boosting Method for Classification of Impervious Surfaces. The International Archives of the Photogrammetry Remote Sensing and Spatial Information Sciences. 2016;XLI-B7:981-5.

[5] Omurakunova G, Bao A, Xu W, Duulatov E, Jiang L, Cai P, et al. Expansion of Impervious Surfaces and Their Driving Forces in Highly Urbanized Cities in Kyrgyzstan. International Journal of Environmental Research and Public Health. 2020;17(1):362.

[6] Dong X, Meng Z, Wang Y, Zhang Y, Sun H, Wang Q. Monitoring Spatiotemporal Changes of Impervious Surfaces in Beijing City Using Random Forest Algorithm and Textural Features. Remote Sensing. 2021;13(1):153.
[7] Tian Y, Chen H, Song Q, Zheng K. A Novel Index for Impervious Surface Area Mapping: Development and Validation. Remote Sensing. 2018;10(10):1521.
[8] Liang X, Lin Y, Zhang H. Mapping Urban Impervious Surface With an Unsupervised Approach Using Interferometric Coherence of SAR Images. Ieee Journal of Selected Topics in Applied Earth Observations and Remote Sensing. 2022;15:2734-44.
[9] Long X, Shao Z, Feng X. Urban Impervious Surface Extraction Based on Remote Sensing Images. The International Archives of the Photogrammetry Remote Sensing and Spatial Information Sciences. 2020;XLII-3/W10:357-60.
[10] Qiao K, Zhu W, Hu D, Hao M, Chen S, Cao S. Examining the Distribution and Dynamics of Impervious Surface in Different Function Zones in Beijing. Journal of Geographical Sciences. 2018;28(5):669-84.
[11] Hidayati IN, Suharyadi R. A Comparative Study of Various Indices for Extraction Urban Impervious Surface of Landsat 8 OLI. Forum Geografi. 2019;33(2):162-72.
[12] Liu H, Deng L, Dou Y, Zhong X, Qian Y. Pansharpening Model of Transferable Remote Sensing Images Based on Feature Fusion and Attention Modules. Sensors. 2023;23(6):3275.
[13] Li Z, Cheng C. A CNN-Based Pan-Sharpening Method for Integrating Panchromatic and Multispectral Images Using Landsat 8. Remote Sensing. 2019;11(22):2606.
[14] Ghayour L, Neshat A, Paryani S, Shahabi H, Shirzadi A, Chen W, et al. Performance Evaluation of Sentinel-2 and Landsat 8 OLI Data for Land Cover/Use Classification Using a Comparison Between Machine Learning Algorithms. Remote Sensing. 2021;13(7):1349.
[15] Khateri M, Shabanzade F, Mirzapour F, Zaji AH, Liu Z. A Variational Approach for Fusion of Panchromatic and Multispectral Images Using a New Spatial–Spectral Consistency Term. Ieee Journal of Selected Topics in Applied Earth Observations and Remote Sensing. 2020;13:3421-36.
[16] Taktak F, Ilı M. Güneş enerji santrali (GES) geliştirme: Uşak örneği. Geomatik. 2018;3(1):1-21.
[17] Laben CA, Brower BV. Process for enhancing the spatial resolution of multispectral imagery using pan-sharpening. Google Patents; 2000.
[18] Maurer T. How to pan-sharpen images using the gram-schmidt pan-sharpen method–A recipe. The International Archives of the Photogrammetry, Remote Sensing and Spatial Information Sciences. 2013;40:239-44.
[19] Li H, Jing L, Tang Y. Assessment of Pansharpening Methods Applied to WorldView-2 Imagery Fusion. Sensors. 2017;17(1):89.
[20] Sarp G. Spectral and Spatial Quality Analysis of Pan-Sharpening Algorithms: A Case Study in Istanbul. European Journal of Remote Sensing. 2014;47(1):19-28.
[21] García FC, Pesántez-Cobos P, Alonso-Sarría F. fusionImage: An R Package for Pan-sharpening Images in Open Source Software. Transactions in Gis. 2020;24(5):1185-207.
[22] Rokni K. Investigating the Impact of Pan Sharpening on the Accuracy of Land Cover Mapping in Landsat Oli Imagery. Geodesy and Cartography. 2023;49(1):12-8.
[23] Kesikoglu MH, Atasever UH, Dadaser-Celik F, Ozkan C. Performance of ANN, SVM and MLH techniques for land use/cover change detection at Sultan Marshes wetland, Turkey. Water Science and Technology. 2019;80(3):466-77.
[24] Jammalamadaka S, Cherukuri AK. Insights Into Quantum Support Vector Machine. 2024.
[25] Li H, Zhou P, Zhang Z. An Investigation Into Machine Pattern Recognition Based on Time-Frequency Image Feature Extraction Using a Support Vector Machine. Proceedings of the Institution of Mechanical Engineers Part C Journal of Mechanical Engineering Science. 2010;224(4):981-94.
[26] Wu A, Zhu J, Yang Y, Liu X, Wang X, Wang L, et al. Classification of Corn Kernels Grades Using Image Analysis and Support Vector Machine. Advances in Mechanical Engineering. 2018;10(12).
[27] Danoedoro P, Gupita DD. Combining Pan-Sharpening and Forest Cover Density Transformation Methods for Vegetation Mapping Using Landsat-8 Satellite Imagery. International Journal on Advanced Science Engineering and Information Technology. 2022;12(3):881.

[28] Farhadi M, Hoshyarmanesh H. Comparison of Image Fusion Techniques Using Worldview-3 Data. 2020.
[29] Park H, Kim N-K, Park S, Choi J. Sharpening of Worldview-3 Satellite Images by Generating Optimal High-Spatial-Resolution Images. Applied Sciences. 2020;10(20):7313.
[30] Alcaras E, Parente C. The Effectiveness of Pan-Sharpening Algorithms on Different Land Cover Types in GeoEye-1 Satellite Images. Journal of Imaging. 2023;9(5):93.

MIM Research Group Research & Design
www.jrede.org

Research Article

SEM images of carbon nanotubes (CNTs): effect of voltage and spot size on image resolutions

Atike Ince Yardimci[1a], Yaser Acikbas*[2b], Rifat Capan[3c]

[1]*Technology Transfer Office, Usak University, Usak, Turkey*
[2]*Department of Electrical and Electronics Engineering, Usak University, Usak, Turkey*
[3]*Department of Physics, Balıkesir University, Balıkesir, Turkey*

Article Info

Article History:

Received: 16 Nov 2024

Accepted: 5 Dec 2024

Keywords:

Carbon nanotube;

Scanning electron microscopy;

High resolution;

Imaging;

Accelerating voltage;

Spot size

Abstract

Scanning electron microscopy (SEM) is a method used to characterize 2D and 3D materials morphologically. It is of great importance with its high resolution, especially in the characterization of nano- and micro-sized materials. In this study, carbon nanotubes (CNTs) were analyzed with SEM, and high-quality images were obtained. With SEM analysis, it can be seen whether carbon nanotubes are formed in a regular structure or not, and whether there are agglomerations or distortions in the structure and could also be utilized to quantify the degree of purity within samples. The diameters of carbon nanotubes can be measured using SEM images. This study obtained the best imaging parameters by taking many SEM images at different magnifications under 3.5 and 7 kV voltage and 2, 2.5, and 3 spot values. The results showed that in the characterization of CNTs by SEM, low spot and low voltage values are more suitable for detailed surface morphology imaging and obtaining high resolution.

1. Introduction

Scanning electron microscopy (SEM) is a microscopy technique that uses electron beams to examine high-resolution images and detailed surface morphologies of samples [1]. Compared to optical microscopy, it is a type of electron microscopy that allows obtaining much higher resolution images thanks to electron beams, and its resolution can vary from 1 nanometer to several nanometers. In this technique a focused electron beam is sent onto the surface of a sample and the surface scans with this electron beam collects the signals coming from the surface with its detectors and converts them into an image. Electrons interact with atoms on the sample surface and produce various signals that can be used to obtain information about surface morphology and composition. There are two main detectors used in SEM for image formation. The first of them is called the secondary electron (SE) detector, the other is the backscattered electron detector. They are the most common detectors used for high-resolution imaging in the SEM measurements. Besides, an energy dispersive X-ray spectroscopy (EDS) detector is used in SEM to examine the surface composition.

SEM is widely used in many disciplines to analyze many different materials [2-5]. It can analyze organic and inorganic substances from nanometer (nm) to micrometer (μm) size [6]. Using SEM, images can be taken from material surfaces with high precision, at a magnification of approximately 300.000x, and even up to 1.000.000X magnification in

*Corresponding author: yaser.acikbas@usak.edu.tr
[a]orcid.org/0000-0001-5482-4230; [b]orcid.org/0000-0003-3416-1083; [c]orcid.org/0000-0003-3222-9056;
DOI: http://dx.doi.org/10.17515/rede2024.004en1116rs

some devices [7]. The magnification ratio of a standard SEM device is between 5x and 300.000x [8]. SEM is also a convenient imaging method during the sample preparation process. It can display conductive, insulating, wet, and dry samples with different properties with a variable pressure system [9]. The size of the samples to be imaged in SEM must be up to 200 mm in diameter and 80 mm in height [10]. Insulating samples are generally examined by coating them with gold [11].

Carbon nanotubes (CNTs) have attracted great attention due to their extraordinary electronic, mechanical, and thermal properties [12-14]. The properties of (CNTs) and devices using (CNTs) directly depend on the nanotube's morphological properties, the nanotube's crystallographic properties, and any defects in the structure [15]. Therefore, the characterization of (CNTs) and the determination of their morphology are important for quality control and use in different applications [16].

SEM images of the carbon nanotube (CNT) samples were taken by scanning the surface with a high-energy beam of electrons [17]. By sending an electron to the specimen surface, several signals can be detected [18]. When the primary electron is sent, high energy backscattered electrons appear and the primary electron can be diffracted with large angles. Secondary electrons are generated when these backscattered electrons emerge from the surface [19]. These secondary electrons have energies between 0 and 20 eV and can be attracted to a highly efficient positively charged detector [20]. Comparing the primary electron number, the secondary electron number is high and increases as the angle φ between the electron beam and the surface normal increases in proportion to $1/\cos\varphi$ [21].

There is a large annular detector below the final lens, facing toward the sample, and this detector can collect a proportion of the scattered electron signal [22]. With increasing atomic number Z of an elemental sample, the scattering of primary electrons increases [23]. Depending on the surface composition and orientation between the electron beam and surface, the backscattered electron signal from a flat, polished sample provides contrast [24].

The resolution of the backscattered electron image is typically in the range between 0.1-1 μm [25], but it is possible to image very finely spaced regions showing compositional contrast at resolutions down to 2-3 nm using high-brightness guns and efficient backscattered electron detectors. A small high-resolution component in the backscattered signal is generated by incident beam electrons being scattered out of the sample very early in their path. The resolution of the whole backscattered signal can be improved by reducing the beam energy but the detectors become less efficient for the lower energy electrons [26], and so this is not appropriate.

In this study, multi-walled CNTs were synthesized by the chemical vapor deposition (CVD) method and then SEM images of these nanotubes were taken under different voltage and spot values. The effects of voltage and spot-on SEM imaging of CNTs were investigated to obtain images of CNTs with high quality and high resolution.

2. Materials and Methods

2.1 CNT Growth Process with Thermal Chemical Vapor Deposition (TCVD) Method

In this study, the TCVD method was utilized to synthesize CNTs (Lindberg/Blue M 1100 ^{o}C Split Mini Furnace) [27]. 50 mg Co-Mo/MgO powder catalyst placed in a quartz boat was transferred into the TCVD system. Initially, a catalyst pretreatment process was carried out under H_2 atmosphere with a flow rate of 200 sccm for 1 hour at 850 ^{o}C to reduce metal oxide particles and prevent amorphous carbon formation for high-quality CNT growth.

After the pretreatment process, the temperature was increased up to 1000 ^{o}C at a rate of 5 ^{o}C/min, and CNT growth was started at 1000 ^{o}C by opening CH_4 gas with a flow rate of 50 sccm. CNT synthesis took 60 min at this growth temperature under 200 sccm H_2 and 50 sccm CH_4 gases at atmospheric pressure.

After the CNT growth process, CH_4 gas was turned off. The system temperature was set to 0 ^{O}C and the system and synthesized CNTs was left to cool under H_2 atmosphere.

2.2 Morphological Characterization of CNTs with SEM

SEM is one of the most widely used tools for analyzing the morphology and size of CNTs in powder form. Its popularity stems from its simplicity and suitability for routine use, offering an advantage over other microscopy methods. SEM can easily be employed to assess the general structure of CNT samples, determine their purity, dimensions, and their orientations [28-30]. Diameters of CNTs also can be measured roughly using SEM results.

In this study, to take SEM images of CNTs, CNTs in powder form were fixed by gluing them to double-sided carbon tape. No coating or pretreatment was applied to image CNTs, and imaging was done as an as-grown form of CNTs. A SE detector was used to image CNTs, and voltage values of 3, 5, and 7 kV and a spot values of 2, 2.5, and 3 were scanned to obtain high-resolution images.

The SEM utilized for this study was a FEI QUANTA 250 FEG. A schematic representation of SEM characterization of CNTs is given in Fig.1.

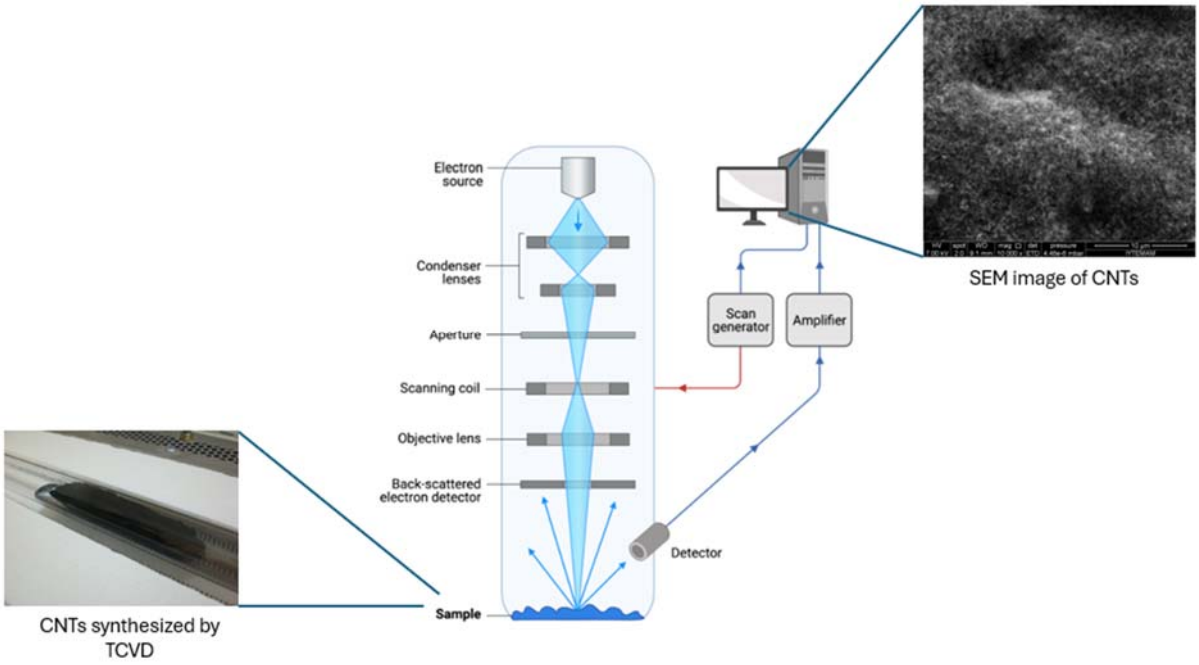

Fig. 1. Schematic representation of SEM characterization of CNTs

3. Results and Discussion

In imaging CNTs in SEM microscopy, the contrast created by the nanotubes provides imaging. The image is formed with the information received from the secondary electrons reflected from the nanotubes and, in some regions, from the catalyst particles remaining during nanotube synthesis [31].

In literature, it is reported that when using tungsten filament SEM, the voltage value should be between 2-10 kV to prevent the sample from charging and to obtain the image of (CNTs)

in high-resolution [30]. In the present study, voltage values of 3, 5, and 7 kV were tried obtain high-resolution CNT images.

SEM pictures of the as-grown CNTs taken under 3 kV accelerating voltage at different spot values and different magnifications are given in Fig. 2 and Fig. 3. SEM images of nanotubes showed that CNTs synthesized by TCVD method under H_2 environment were high purity and high quality. SEM images of CNTs were taken at increasing magnifications: 25.000x, 50.000x, and 100.000x. In this way, it is possible to obtain information about the general morphology of the CNT sample and to closely examine the morphology of a single nanotube. General images taken from further away, especially nanotube bundles in the powder CNT sample, can be observed and examined whether they contain irregular structures. The purity level of the nanotubes can be seen. In close-up images taken at 100.000X and higher magnifications, nanotubes can be observed individually and their diameters can also be measured. To obtain an accurate value for diameter measurement, the diameter of at least 50 nanotubes from the same sample must be measured and averaged.

When SEM images taken under 3 kV voltage and 2.5 spot value are examined, carbon nanotube bundles can be clearly observed under 25000X magnification (Fig. 2). As the magnification increases, nanotubes become more evident and nontangled CNTs formed in a regular structure are observed. The image quality at these voltage and spot values was considered suitable for CNT imaging.

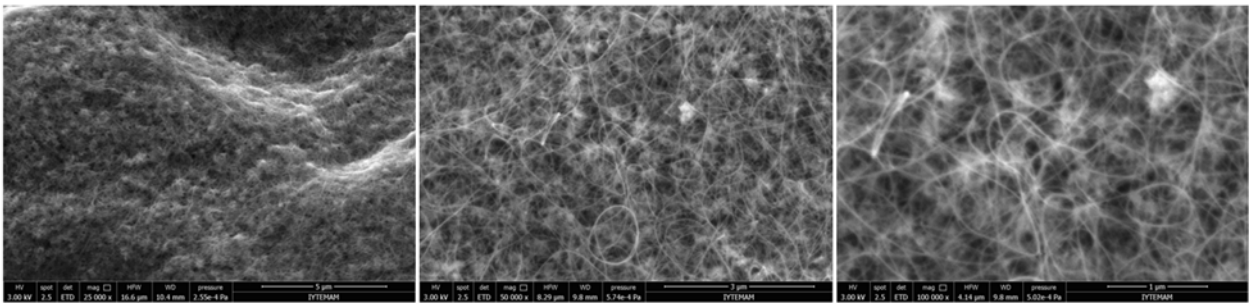

Fig. 2. SEM images of CNTs under 3 kV accelerating voltage, 2.5 spot value at 25.000, 50.000, and 100.000X.

In SEM, spot value refers to the diameter of the electron beam used during imaging. Spot plays an important role in observing resolution and details in SEM imaging. A lower spot value means a thinner, more concentrated electron beam. These results in higher resolution and sharper, more detailed images. Therefore, low spot values are more suitable for observing fine structures, surface features, or small particles. Higher spot values result in a larger diameter electron beam. Under high spotlight, the resolution of the image decreases but increases the depth of field; this can be useful when imaging larger or deeper structures.

When we increased the spot value from 2.5 to 3 while the 3 kV voltage was constant, the contrast between the nanotubes and the ground increased, but it was observed that the depth decreased compared to the SEM images taken under 2.5 spot (Fig. 3).

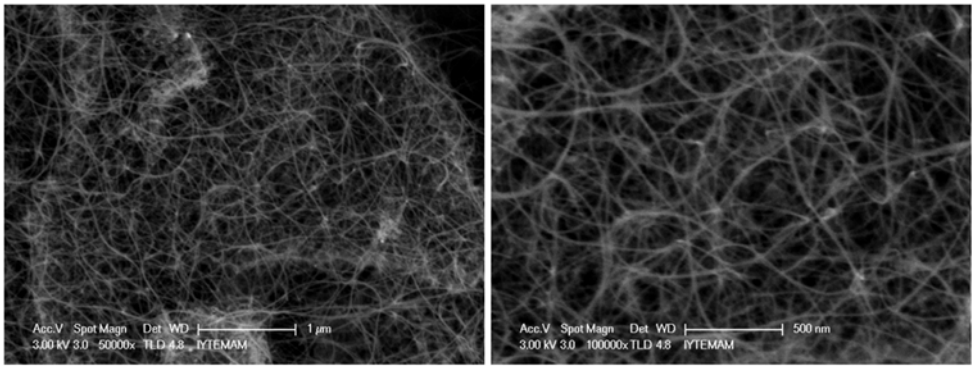

Fig. 3. SEM images of CNTs under 3 kV accelerating voltage, 3 spot values at 50.000, and 100.000X.

In SEM, accelerating voltage is a significant parameter that directly affects imaging. Voltage controls the energy of the electron beam. High voltage increases the energy of the electron beam, which can lead to decreased resolution due to the increased interaction volume of electrons within the sample. Therefore, higher voltage may reduce the resolution of fine details on the surface of the sample.

Lower voltage values result in lower energy electrons interacting more superficially with the sample. The interaction volume is smaller, providing better resolution for surface details. At the same time, lower voltage results in shallower penetration; This is advantageous for surface-sensitive imaging where surface properties are of primary interest.

SEM images taken under 5 kV accelerating voltage at different spot values were given in Fig. 4 and Fig. 5. As expected, it can be seen that SEM images taken under 5 kV voltage provide less detail compared to SEM images taken under 3 kV voltage. Especially in more general images at 25000X magnification, it is seen that the details on the surface decrease and the resolution decreases with the increase in voltage (Fig. 4).

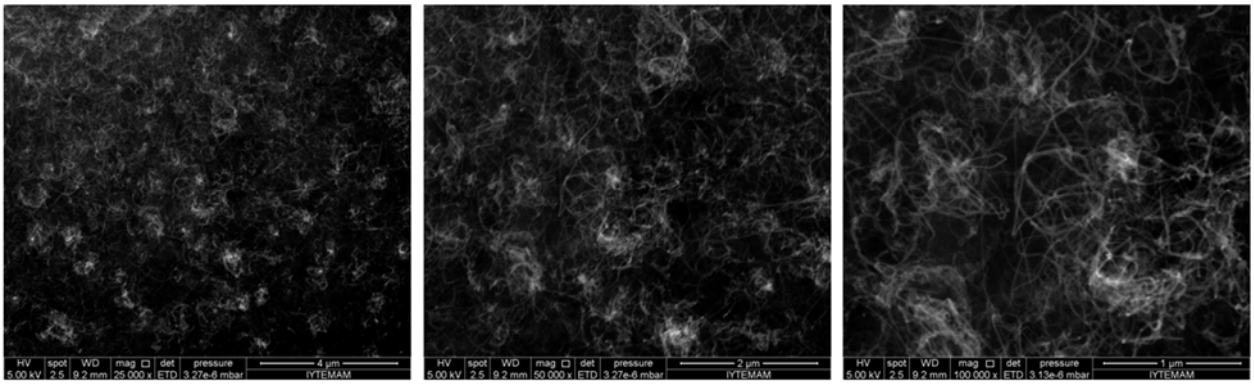

Fig. 4. SEM images of CNTs under 5 kV accelerating voltage, 2.5 spot value at 25.000, 50.000, and 100.000X.

A lower spot size typically results in a weaker signal. Under low spot, the electron beam is focused more into a smaller area, resulting in a lower signal-to-noise ratio. A larger spot provides a larger interaction area, thus increasing the intensity of the signal; this can be useful for capturing clearer images in less time. When the spot value was increased from 2.5 to 3 under 5 kV voltage, it was observed that the contrast increased and the surface details decreased, as in the images taken under 3 kV (Fig. 5).

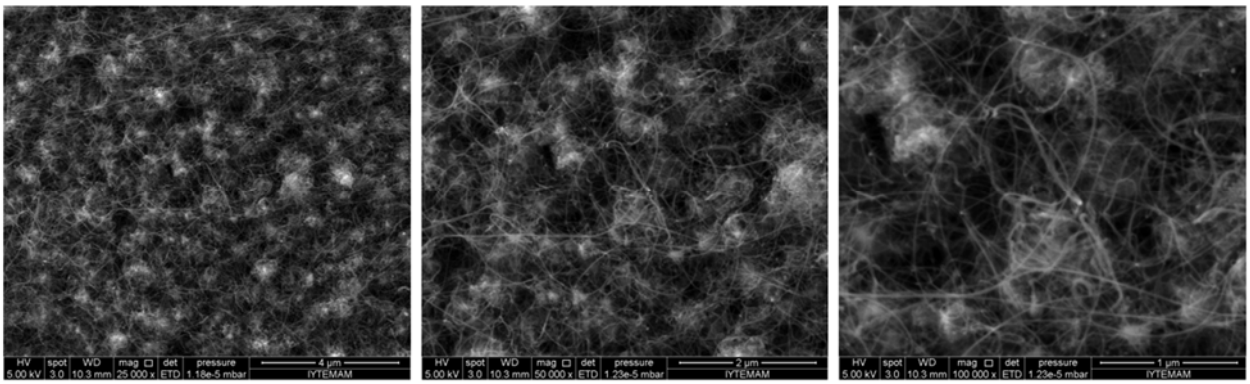

Fig. 5. SEM images of CNTs under 5 kV accelerating voltage, 3 spot value at 25.000, 50.000, and 100.000X.

While it was expected that the details would decrease further at high voltage after the voltage increased to 7 kV, by reducing the spot value to 2, high-quality SEM images of CNTs with high resolution and excellent surface details were obtained. Therefore, the effect of low spot value on image quality is shown in Fig. 6 was also clearly observed.

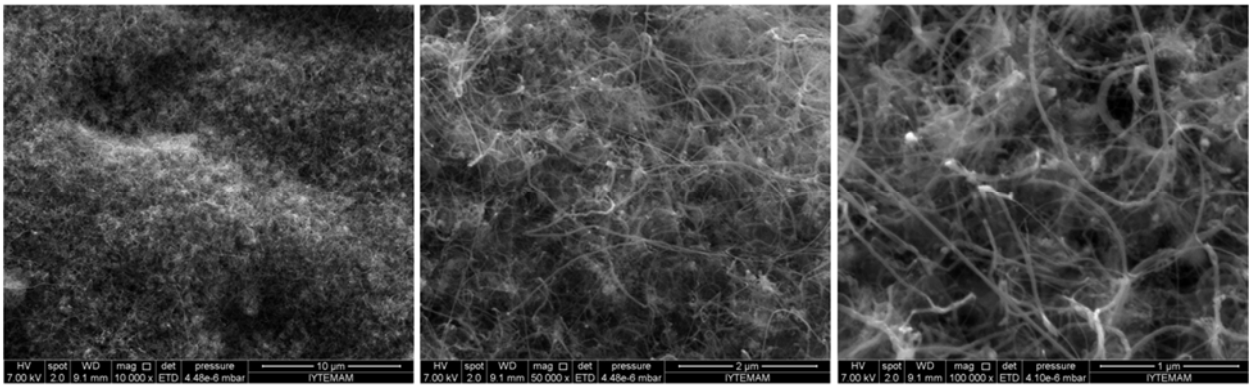

Fig. 6. SEM images of CNTs under 7 kV accelerating voltage, 2 spot values at 25.000, 50.000, and 100.000X.

Since the beam is highly focused on a smaller area with a smaller spot size, it may cause heating in the imaged area and burn in sensitive samples. However, a higher spot value distributes the energy over a wider area, reducing the risk of damage, but reducing image clarity. As a result of the spot value increasing to 2.5 while the voltage remains the same (7 kV), it is seen that there is charging in the regions where the CNT clusters are located, causing excessive brightness. Therefore, CNT clusters cannot be observed clearly (Fig. 7).

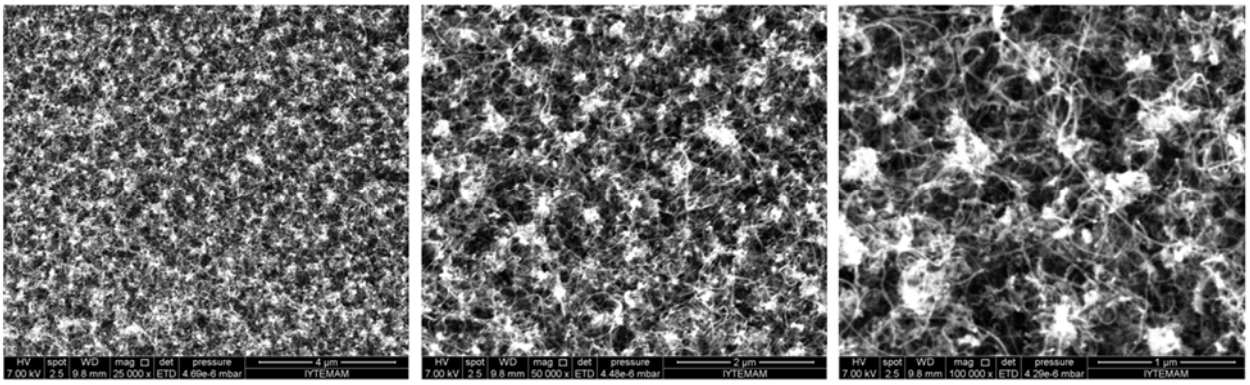

Figure 7: SEM images of CNTs under 7 kV accelerating voltage, 2.5 spot value at 25.000, 50.000, and 100.000X.

Also, using a low spot value may require slower scanning speeds to achieve the same signal strength, potentially increasing imaging time. A larger spot size can speed up imaging due to the stronger signal. Compared to Fig. 7, after the spot value was increased from 2 to 2.5 at 7 kV accelerating voltage value, the charging effect on the image became clear. CNTs are not clearly visible. Even at 100.000X magnification, individual CNTs are very difficult to observe (Fig. 8).

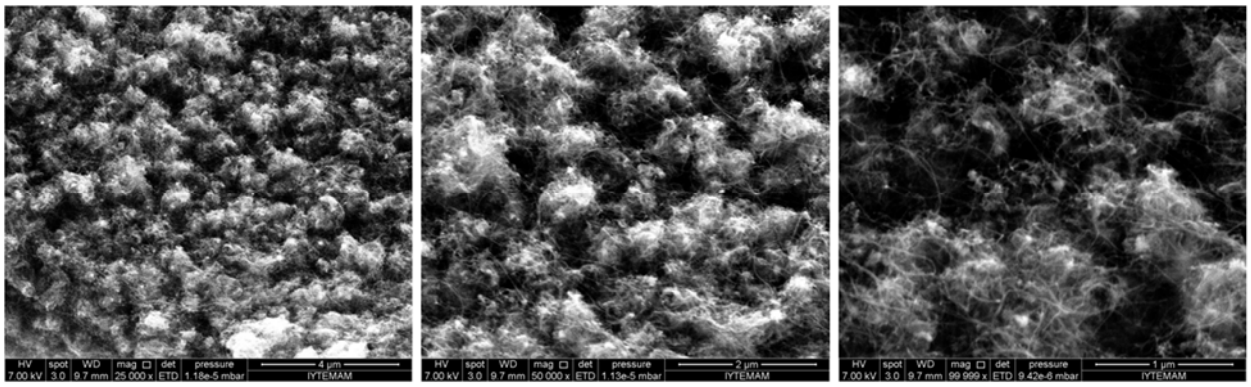

Figure 8: SEM images of CNTs under 7 kV accelerating voltage, 3 spot value at 25.000, 50.000, and 100.000X.

4. Conclusions

In this study, the morphologies of CNTs synthesized by the TCVD method on Co-Mo/MgO powder catalyst were examined by SEM technique. The effects of voltage and spot values at different magnifications were examined to obtain high-resolution CNT images and detailed surface morphology. The results showed that CNTs can be easily imaged in SEM in their as-grown form without any coating.

In SEM imaging, the spot size affects the balance between resolution, signal intensity, imaging speed, and sample preservation. Choosing the optimal spot value depends on the specific requirements of the analysis, such as the level of detail needed and the characteristics of the sample. When the effects of voltage are examined, at high voltage values, electrons penetrate deep into the material surface with their high energy. Therefore, less surface detail can be captured, and more contrast occurs, and very high voltages can damage the sample. At lower voltage values, electrons penetrate the surface less and these voltage values are more suitable for seeing surface details. Therefore, while lower voltage provides higher resolution, it is also less likely to damage the sample. In addition, the choice of voltage and spot values depends on the requirements such as sample type, desired resolution, and level of detail needed.

In here, SEM images of CNTs were taken between 3-7 kV and 2-3 spot size and as a conclusion, the most appropriate accelerating voltage and spot size combination for SEM analysis of CNTs among the examined parameters was found as accelerating of 3kV and spot size of 2.5 with more CNT surface information and details.

References

[1] Vladár, A.E. and Hodoroaba, V.-D. Characterization of nanoparticles by scanning electron microscopy, in Characterization of nanoparticles. 2020; 7-27.

[2] Ali, A., Zhang, N., and Santos, R.M. Mineral characterization using scanning electron microscopy (SEM): a review of the fundamentals, advancements, and research directions. Applied Sciences, 2023; 13(23): 12600.
[3] Priks, H. and Butelmann, T. Scanning electron microscopy (SEM) protocol for imaging living materials. 2020.
[4] Hashimoto, Y., Nagaoka, Y., Aiso, T., Yabu, S., and Sasajima, M. Investigation of Ultra-Low-Voltage SEM Imaging Method of Battery Materials. 2024, Oxford University Press US.
[5] Thuan, N.D., Cuong, H.M., Nam, N.H., Huong, N.T.L., and Hong, H.S. Morphological analysis of Pd/C nanoparticles using SEM imaging and advanced deep learning. RSC advances, 2024; 14(47): 35172-35183.
[6] Ribeiro, J., DaBoit, K., Flores, D., Kronbauer, M.A., and Silva, L.F. Extensive FE-SEM/EDS, HR-TEM/EDS and ToF-SIMS studies of micron-to nano-particles in anthracite fly ash. Science of the total environment, 2013; 452: 98-107.
[7] QUNTUM, R., SYNTHESIS OF ZEOLITE-A FROM PUMICE SILICA AND ALUMUNIUM FOIL AS A CATALYST FOR PYROLYSIS OF PALM OIL MILL EFFLUENT (POME). 2023.
[8] Mohammed, A. and Abdullah, A. Scanning electron microscopy (SEM): A review. in Proceedings of the 2018 International Conference on Hydraulics and Pneumatics—HERVEX, Băile Govora, Romania. 2018.
[9] Donald, A.M. The use of environmental scanning electron microscopy for imaging wet and insulating materials. Nature materials, 2003; 2(8): 511-516.
[10] Echlin, P., Handbook of sample preparation for scanning electron microscopy and X-ray microanalysis. 2011: Springer Science & Business Media.
[11] Juhász, L., Moldován, K., Gurikov, P., Liebner, F., Fábián, I., Kalmár, J., and Cserháti, C. False morphology of aerogels caused by gold coating for SEM imaging. Polymers, 2021; 13(4): 588.
[12] Han, Z. and Fina, A. Thermal conductivity of carbon nanotubes and their polymer nanocomposites: A review. Progress in polymer science, 2011; 36(7): 914-944.
[13] Gupta, N., Gupta, S.M., and Sharma, S. Carbon nanotubes: Synthesis, properties and engineering applications. Carbon Letters, 2019; 29: 419-447.
[14] Wu, Y., Zhao, X., Shang, Y., Chang, S., Dai, L., and Cao, A. Application-driven carbon nanotube functional materials. ACS nano, 2021; 15(5): 7946-7974.
[15] Banerjee, S. and Kar, K.K. Characteristics of carbon nanotubes. Handbook of nanocomposite supercapacitor materials I: characteristics, 2020; 179-214.
[16] Soni, S.K., Thomas, B., and Kar, V.R. A comprehensive review on CNTs and CNT-reinforced composites: syntheses, characteristics and applications. Materials Today Communications, 2020; 25: 101546.
[17] Homma, Y., Suzuki, S., Kobayashi, Y., Nagase, M., and Takagi, D. Mechanism of bright selective imaging of single-walled carbon nanotubes on insulators by scanning electron microscopy. Applied Physics Letters, 2004; 84(10): 1750-1752.
[18] Goldstein, J. Practical scanning electron microscopy: electron and ion microprobe analysis. 2012: Springer Science & Business Media.
[19] Zaefferer, S. and Habler, G. Scanning electron microscopy and electron backscatter diffraction. 2017.
[20] Schenkel, T., Hamza, A., Barnes, A., and Schneider, D. Interaction of slow, very highly charged ions with surfaces. Progress in Surface Science, 1999; 61(2-4): 23-84.
[21] O'Connor, D.J., Sexton, B.A., and Smart, R.S. Surface analysis methods in materials science. 2013; 23. Springer Science & Business Media.
[22] Spence, J.C. High-resolution electron microscopy. 2013: OUP Oxford.
[23] Inkson, B.J. Scanning electron microscopy (SEM) and transmission electron microscopy (TEM) for materials characterization, in Materials characterization using nondestructive evaluation (NDE) methods. 2016, 17-43.
[24] Brodusch, N., Demers, H., and Gauvin, R. Imaging with a commercial electron backscatter diffraction (EBSD) camera in a scanning electron microscope: A review. Journal of Imaging, 2018; 4(7): 88.
[25] Reimer, L., Transmission electron microscopy: physics of image formation and microanalysis. 2013; 36 Springer.

[26] Faruqi, A. and Henderson, R. Electronic detectors for electron microscopy. Current opinion in structural biology, 2007; 17(5): 549-555.
[27] Yardimci, A.I., Yılmaz, S., and Selamet, Y. The effects of catalyst pretreatment, growth atmosphere and temperature on carbon nanotube synthesis using Co–Mo/MgO catalyst. Diamond and Related Materials, 2015; 60: 81-86.
[28] Sun, X., Chen, T., Yang, Z., and Peng, H. The alignment of carbon nanotubes: an effective route to extend their excellent properties to macroscopic scale. Accounts of chemical research, 2013; 46(2): 539-549.
[29] Wang, B.N., Bennett, R.D., Verploegen, E., Hart, A.J., and Cohen, R.E. Quantitative characterization of the morphology of multiwall carbon nanotube films by small-angle X-ray scattering. The Journal of physical chemistry C, 2007; 111(16): 5859-5865.
[30] Lehman, J.H., Terrones, M., Mansfield, E., Hurst, K.E., and Meunier, V. Evaluating the characteristics of multiwall carbon nanotubes. Carbon, 2011; 49(8): 2581-2602.
[31] Huang, L., Zhang, D., Zhang, F.H., Feng, Z.H., Huang, Y.D., and Gan, Y. High-contrast SEM imaging of supported few-layer graphene for differentiating distinct layers and resolving fine features: there is plenty of room at the bottom. Small, 2018; 14(22): 1704190.

Research & Design

In This Issue

MIM Research & Publishing